Recent increase of Saharan dust transport over the Mediterranean Sea, as revealed from ocean color satellite (SeaWiFS) observations

D. Antoine, D. Nobileau

HAL Id: hal-03494182
https://hal.science/hal-03494182

Submitted on 19 Dec 2021

Recent increase of Saharan dust transport over the Mediterranean Sea, as revealed from ocean color satellite (SeaWiFS) observations

D. Antoine[1] and D. Nobileau[1]

[1] An algorithm was previously developed and validated, which is capable of detecting blue-absorbing aerosols from near infrared and visible remote-sensing observations, as they are in particular collected by satellite ocean color sensors. This algorithm has been applied to 7 years (1998–2004) of Sea-Viewing Wide Field-of-View Sensor (SeaWiFS) observations over the Mediterranean Sea, on the one hand to further illustrate the appropriateness of ocean color observations to provide relevant information about aerosol types and in particular absorbing aerosols, and, on the other hand, to describe the seasonal and interannual variability of Saharan dust over the Mediterranean Sea during the SeaWiFS era. This extensive application allowed the validation of the retrieved aerosol optical thickness to be more thoroughly performed, thanks to data from the Aerosol Robotic Network (AERONET). The results of this validation and the mapping of dust aerosols and of the associated optical thickness demonstrate the skill of the algorithm. These results are in agreement with, and provide a complement to, the results of previous studies based on other remote sensing techniques, which were applied to data from the 1980s and early 1990s. They also show an increase of the dust transport over the Mediterranean over the 1998-to-2004 time period.

Citation: Antoine, D., and D. Nobileau (2006), Recent increase of Saharan dust transport over the Mediterranean Sea, as revealed from ocean color satellite (SeaWiFS) observations, *J. Geophys. Res.*, *111*, D12214, doi:10.1029/2005JD006795.

1. Introduction

[2] The interest taken in the study of desert dust originates in its potential effect on the radiative budget and climate of the whole planet [e.g., *Charlson et al.*, 1992; *Li et al.*, 1996]. Large-scale effects are expected because Saharan or Asian dust affect extended regions far from their sources [e.g., *Prospero and Carlson*, 1972; *Savoie and Prospero*, 1977; *Li et al.*, 1996; *Kaufman et al.*, 2005] and because their amount in the atmosphere may have increased largely because of human activity [*Andreae*, 1996]. A large uncertainty remains, however, about the sign and magnitude of the radiative forcing of aerosols, and in particular of dust aerosols [*Intergovernmental Panel on Climate Control* (*IPCC*), 2001]. This uncertainty is primarily caused by an insufficient knowledge of the absorption properties of these aerosols [e.g., *Bellouin et al.*, 2003; *Tanré et al.*, 2003].

[3] Another effect of dust aerosols could be to either fertilize the upper oceanic layers by releasing nutrients or iron adsorbed onto their surface [e.g., *Donaghay et al.*, 1991; *Duce et al.*, 1991] or to deplete surface waters of phosphorus, a possible "feeding" source of phytoplankton,

by carrying it away through adsorption and sinking [*Krom et al.*, 1991]. Therefore there is undoubtedly a connection between dust and phytoplankton [e.g., *Stegman*, 2000], although the reasons for this link remain largely unexplained.

[4] Dust aerosols also modify cloud microphysical properties [e.g., *Levin and Ganor*, 1996], can influence rain acidity [*Loÿe-Pilot et al.*, 1986] and can affect atmospheric convection [e.g., *Brooks and Legrand*, 2000]. The identification of desert dust occurrences over the ocean, and the quantification of the associated burden, are therefore important missions. The residence time of aerosols in the atmosphere, and in particular of mineral dusts, is however of only a few days, so their distribution is highly variable in space and time. This is the reason why remote sensing of desert aerosols has increasingly developed, as the best technique to catch individual events (aerosol "plumes") and to integrate them into regional or global pictures of the aerosol transport.

[5] Remote sensing of aerosols has a long history, and a wide range of techniques have been developed in the past 20 years, using various sensors and various parts of the electromagnetic spectrum (see reviews of, e.g., *Kaufman et al.* [1997], *King et al.* [1999], and *Kaufman et al.* [2002]). It is more recently that ocean color has been incorporated into the panoply of methods considered as capable of providing reliable information about the amounts and types of aerosols (but see, e.g., *Moulin et al.* [2001a] and *Wang et al.* [2000]). This late consideration is simply due to the fact that the main concern of the ocean color science is actually to get

[1] Laboratoire d'Océanographie de Villefranche, Observatoire Océanologique de Villefranche, CNRS/Université Pierre et Marie Curie-Paris 6, Villefranche sur mer, France.

rid of the aerosol effect on the recorded signal, i.e., the atmospheric correction, rather than studying aerosols themselves.

[6] The term ocean color actually means the observation of the spectral reflectance of the sea in the visible to near infrared domains, which is precisely where aerosols play a role and can be detected. In addition, ocean color is extremely demanding in terms of accuracy of the retrieved water-leaving reflectances, and in particular in the blue part of the spectrum [*Gordon*, 1990, 1997]. For the modern sensors, it has been necessary to drastically improve the atmospheric correction schemes as compared to what was done in the 1980s [*Gordon*, 1997] with the Coastal Zone Color Scanner (CZCS) [e.g., *Gordon*, 1978]. This was achieved by improving the direct and vicarious radiometric calibration of the sensors [e.g., *Barnes et al.*, 2001], by using a larger number of channels (in the near infrared in particular), and by using aerosol models to describe the spectral dependence of the atmospheric signal and in particular the multiple scattering effects. It is through this process that the by-products of the atmospheric correction of ocean color observations were improved and became relevant to aerosol science. Regional to large-scale quantitative assessment of aerosols over the ocean, and in particular of desert dust, is now within reach either using historical data sets (e.g., the CZCS [*Stegman and Tindale*, 1999]) or using the new generation of ocean color remote sensors such as Sea-Viewing Wide Field-of-View Sensor (SeaWiFS) [*Jamet et al.*, 2004; *Stegman*, 2004a, 2004b; *Wang et al.*, 2005], Moderate Resolution Imaging Spectroradiometer (MODIS) [*Barnaba and Gobbi*, 2004; *Kaufman et al.*, 2005; *Remer et al.*, 2005], Medium Resolution Imaging Spectrometer (MERIS) [*Nobileau and Antoine*, 2005], or Polarization and Directionality of the Earth's Reflectances (POLDER)-I and –II [e.g., *Boucher and Tanré*, 2000; *Chiapello et al.*, 2000; *Deuzé et al.*, 1999, 2000].

[7] In this context, and in particular within the frame of the development of the atmospheric correction algorithms for the European MERIS ocean color sensor [*Rast et al.*, 1999], a method was developed that is capable of detecting over oceanic waters the presence of blue-absorbing aerosols, in particular desert dusts, and then of determining their optical thickness and Ångstrøm exponent. This algorithm has been described, tested on selected SeaWiFS and MERIS scenes [*Nobileau and Antoine*, 2005], and validated against in situ data from the AERONET [*Holben et al.*, 1998]. This algorithm is similar in spirit, yet simpler in its implementation, to other algorithms previously proposed to cope with the case of absorbing aerosols [e.g., *Gordon et al.*, 1997]. In the present work, the *Nobileau and Antoine* [2005] algorithm has been systematically applied to all SeaWiFS observations collected over the Mediterranean Sea from 1998 to 2004.

[8] The first aim is to conclusively demonstrate the applicability of the method when it is applied to large data sets, which include by definition all possible situations in terms of (1) the geometry of observation, (2) the amount and type of aerosols, and (3) the optical properties of the underlying ocean. This demonstration is important in particular because the ultra violet domain and the infrared for wavelengths above ∼1 μm, where specific features of

absorbing aerosols are easier to identify than in the visible (e.g., *Herman et al.* [1997] for the UV), are usually unavailable in the bandset of ocean color sensors. The 400–900 nm range is therefore not optimal in this respect. The existing knowledge about the transport of the dust aerosols over the Mediterranean also provides a good context for the validation of the retrieved aerosol optical thickness and type.

[9] The second aim is the study of the seasonal and interannual variability of Saharan dust over the Mediterranean Sea during the SeaWiFS era, as a complement to previous studies that used single broadband visible information over previous time periods, in particular *Moulin et al.* [1998] who used Meteosat observations from 1983 to 1994 and algorithms developed by *Moulin et al.* [1997a, 1997b].

[10] Some recent studies have suggested that climate variability controls the Saharan dust export [*Moulin et al.*, 1997c; *Brooks and Legrand*, 2000; *Chiapello and Moulin*, 2002; *Moulin and Chiapello*, 2004]. A thorough understanding of the distribution and transport of atmospheric dust aerosol particles is therefore necessary to understand this interaction. Long-term time series are also desirable if the interactions and feedbacks between climate and aerosols are to be understood. The SeaWiFS record is, from this point of view, an invaluable data source.

2. Data (SeaWiFS) and Method

[11] Data from the SeaWiFS sensor [*Hooker et al.*, 1992] have been continuously collected by NASA since its launch by Orbital Science Corporation (OSC) in September of 1997. The so-called Level-1a data have been converted into Level-1b, i.e., top-of-atmosphere (TOA) calibrated total radiances in eight spectral bands from 412 to 865 nm, using SeaWiFS Data Analysis System (SeaDAS) [*Fu et al.*, 1998] version 4.4 and the calibration file delivered in 2003. The full set of 4-km Global Area Coverage (GAC) data available from 1998 to 2004 for the Mediterranean Sea, i.e., about 6700 images, have been processed with the algorithm summarized below. Only specific features relevant to the present regional application are briefly recalled, and the reader is referred to the references therein for more detailed information.

[12] The reflectance is first defined because it is the quantity in use for the rest of the paper

$$\rho(\lambda, \theta_s, \theta_v, \Delta\varphi) = \pi L(\lambda, \theta_s, \theta_v, \Delta\varphi) / F_0(\lambda)\mu_s \quad (1)$$

where L is radiance (W m^{-2} nm^{-1} sr^{-1}), F_0 is the extraterrestrial irradiance (W m^{-2} nm^{-1}), θ_s is the Sun zenith angle (cosine is μ_s), θ_v is the satellite viewing angle, and $\Delta\varphi$ is the azimuth difference between the half vertical plane containing the Sun and the pixel and the half vertical plane containing the satellite and the pixel. Because π carries the unit of steradian, the reflectance ρ is dimensionless.

[13] The central difficulty of the atmospheric correction of ocean color observations lies in the identification of the aerosol in presence and the quantification of the multiple scattering effects. All methods in use for the present generation of sensors somehow rely on precomputed signals, coupled to a method allowing navigation in these

signals in order to identify from the near infrared bands the most suitable aerosol to perform the correction of the visible bands [see, e.g., *Gordon*, 1997]. The MERIS algorithm [*Antoine and Morel*, 1999] belongs to this general category of methods. It is a full multiple scattering inversion method, based on aerosol models and precomputed lookup tables (LUTs).

[14] Because only the path reflectances in the near infrared are used by this method (the contribution of the ocean being null in this wavelength domain), it cannot alone discriminate between absorbing and nonabsorbing aerosols, which have similar signatures in this spectral domain. The effect of absorption is only detectable in the visible, where the marine contribution becomes however significant and varying with the chlorophyll content of oceanic waters, which is unknown when starting the atmospheric correction. It is precisely to overcome this difficulty that a specific technique was proposed by *Nobileau and Antoine* [2005]. It basically consists in determining an error budget at one wavelength around 510 nm, based on a first-guess estimation of the atmospheric path reflectance as if the atmosphere was of a maritime type, and on a reasonable hypothesis about the marine signal at this wavelength. The latter is possible because a hinge point exists in the spectrum of the marine reflectance around 510–520 nm [*Clarke et al.*, 1970], so ρ_w is little varying there with the chlorophyll concentration. A mean reflectance and its associated uncertainty can be derived at this wavelength, $\bar{\rho}_w(510)$ and $\sigma(\rho_w)$, respectively, which were assigned fix values, i.e., 1.2×10^{-2} and 3×10^{-3} (but see later). This budget is therefore computed as the total reflectance minus the path reflectance estimated for maritime aerosols minus $\bar{\rho}_w(510)$ minus $\sigma(\rho_w)$. Identification of blue-absorbing aerosols is then achieved when this budget demonstrates a significant overcorrection of the atmospheric signal when using nonabsorbing maritime aerosols, as a footprint of absorption. In the work of *Nobileau and Antoine* [2005], the threshold for identification of absorption at 510 nm was set to -3×10^{-3} in terms of reflectance, which includes the typical accuracy of the correction for maritime aerosols and the typical calibration uncertainty of the sensor. The theoretical detection limit in terms of optical thickness at 865 nm was determined at about 0.15.

[15] It is worth noting that this method cannot discriminate among the most common types of absorbing aerosols (mineral dust, soot, or biomass burning aerosols). Some external information is required in order to assign the detected absorption to a given family of aerosols. In the frame of the present application to the Mediterranean, however, Saharan dust is likely to represent the vast majority of absorbing aerosols.

[16] After absorption has been detected, the atmospheric correction is restarted using specific sets of absorbing aerosol models (i.e., specific LUTs) until the couple of models that minimizes the error budget at 510 nm is found. The aerosol optical thickness at all wavelengths and the Ångstrøm exponent are then derived.

[17] In the first step, a set of 12 aerosol models is used (from *Shettle and Fenn* [1979] and *Gordon and Wang* [1994a]). This set includes four maritime aerosols, four rural aerosols that are made of smaller particles, and four coastal aerosols that are a mixing between the maritime and the rural aerosols. The mean particle sizes of these aerosols, thus their optical properties, are varying as a function of the relative humidity, which is set to 50, 70, 90, and 99% (hence the 3 times four models). This set covers the range of spectral dependencies that may occur over most oceanic areas, from the clearest offshore regions to the more turbid coastal atmospheres. This set of aerosol models is actually the one used in the standard NASA processing of the SeaWiFS observations [*Gordon and Wang*, 1994a]. It has been already validated against in situ observations [*Schwindling et al.*, 1998]. In addition to these boundary-layer aerosols, constant backgrounds are introduced in the free troposphere (2–12 km), with continental aerosol with $\tau = 0.025$ at 550 nm [*World Climate Research Program (WCRP)*, 1986] and the stratosphere (12–30 km), with H_2SO_4 aerosol with $\tau = 0.005$ at 550 nm [*WCRP*, 1986].

[18] The lookup tables specific to absorbing aerosols have been generated with the six dust models and the three vertical distributions proposed by *Moulin et al.* [2001a], which have been derived as the most appropriate to reproduce the TOA total radiances recorded by SeaWiFS above thick dust plumes off western Africa. The mean Ångstrøm exponent of these models is about 0.4 when computed between 443 and 865 nm. When these aerosols are present, a background of maritime aerosol is maintained, using the *Shettle and Fenn* [1979] maritime model for a relative humidity of 90% and an optical thickness of 0.05 at 550 nm [*Kaufman et al.*, 2001]. The backgrounds in the free troposphere and the stratosphere are maintained.

[19] A specific test using the band at 412 nm was developed in order to eliminate clouds without eliminating thick dust plumes (see in the work of *Nobileau and Antoine* [2005]), which are quite bright in the near infrared and therefore are eliminated when using a low threshold in this wavelength domain (as done for instance in the standard processing of the SeaWiFS observations). This test is an alternative to other techniques based on the spatial heterogeneity of the scene [e.g., *Martins et al.*, 2002].

[20] A correction for the whitecaps reflectance is performed following *Gordon and Wang* [1994b], using the National Centers for Environmental Prediction (NCEP) wind speed that is provided as auxiliary data to the SeaWiFS products. The implementation of this technique follows the SeaDAS 4.7 software [*Fu et al.*, 1998].

[21] Finally, because the algorithm has been designed for oceanic Case 1 waters where the contribution of the ocean in the near infrared bands is zero, turbid Case 2 waters, for which the near infrared signal is significant, are screened out by using a threshold on the reflectance at 555 nm, following *Bricaud and Morel* [1987].

[22] In the work of *Nobileau and Antoine* [2005], the adoption of unique values for $\bar{\rho}_w(510)$ and $\sigma(\rho_w)$ was possible in the frame of a demonstration study based on a few selected scenes. For the present regional application, including thousands of scenes and all seasons, the use of single mean values for $\bar{\rho}_w(510)$ and $\sigma(\rho_w)$ has been abandoned. Indeed, the changes of the marine reflectance at 510 nm are minimal yet significant enough so that ignoring them, in particular their seasonal changes, could lead to bias the dust detection.
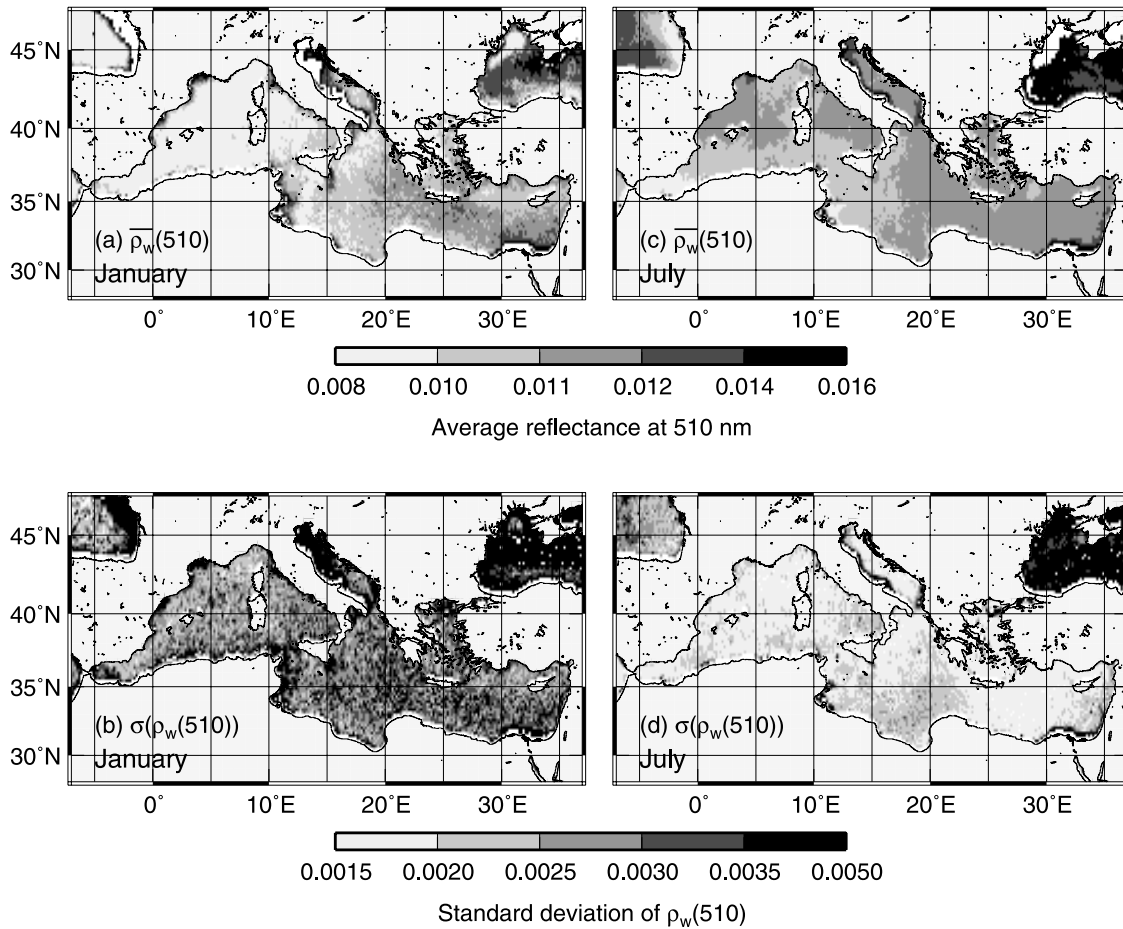
Figure 1. The 7-year (1998–2004) monthly climatology of the average marine reflectance at 510 nm, $\bar{\rho}_w(510)$, and of its standard deviation, $\sigma(\rho_w)$, for the months of (a, b) January and (c, d) July, and as derived from 7 years of standard SeaWiFS level-3 composite data.

[23] A climatology of the monthly average of these two quantities has been therefore derived from 7 years of the standard SeaWiFS level-3 data (1998 to 2004; data from the NASA reprocessing 4), at a spatial resolution of 1/6°, i.e., about half the resolution of the SeaWiFS level-3 "Standard Mapped Images" data. For a given month, the climatological monthly averages have been computed from the seven individual monthly composites, by (1) summing up the seven sums of individual daily values that are provided in the monthly composites (Level-3 "binned" data), (2) summing up the seven corresponding total number of pixels, and (3) dividing both totals to get the average (which is not therefore the mean of the monthly means but the true mean of all individual daily values). The standard deviation was similarly derived from seven monthly values of the sum of squares of the data and over the 7 years so that it includes both a spatial dimension (changes within the 1/6° bin) and a temporal dimension (variability within a month and among the 7 years).

[24] Because the standard NASA atmospheric correction scheme for the SeaWiFS sensor cannot cope with absorbing aerosols, however, an overcorrection of the visible observations occurs when they are present in the atmosphere, leading to underestimated marine reflectances at 510 nm [e.g., *Schollaert et al.*, 2003]. The lowest $\rho_w(510)$ values were therefore reset to a minimum value of 0.008, as empirically determined from in situ observations [see, e.g., *Nobileau and Antoine*, 2005, Figure 3]. Similarly, large values have been put to an upper limit of 0.016, assuming that larger values cannot be found in Case 1 waters. A similar bounding has been applied to $\sigma(\rho_w)$, with extrema of 1.5×10^{-3} and 5×10^{-3}.

[25] Examples of the climatology for the months of January and July are shown in Figure 1. As expected, the changes between these two seasons are low, yet significant enough as regards the error budget at 510 nm to justify the need for using this climatology instead of a unique value. It has been verified for instance that using this climatology avoids erroneous dust identifications in winter and beginning of spring in the northwestern Mediterranean, where the phytoplankton is blooming and the marine reflectance is significantly lower than 1.2×10^{-2} (i.e., the constant value used by *Nobileau and Antoine* [2005]).

[26] When processing a pixel in a 4-km resolution level-1b scene, $\bar{\rho}_w(510)$ and $\sigma(\rho_w)$ are spatially interpolated from the surrounding grid points of the monthly climatology.
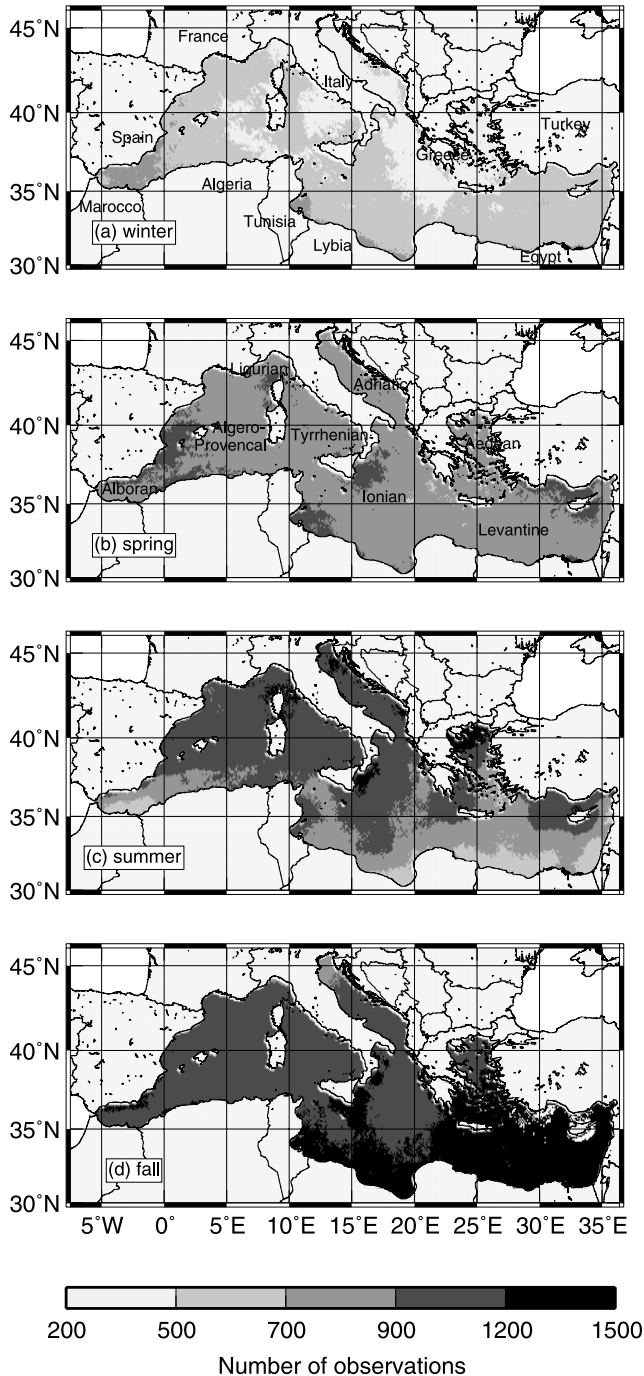
Figure 2. Total number of clear-sky, nonglint, SeaWiFS Global Area Coverage (GAC) observations collected over the Mediterranean Sea from 1998 to 2004 and for the four seasons. The names of the main basins are indicated on Figure 2b.

There is no time interpolation, i.e., the monthly averaged value for a given month is used for all days in this month.

[27] The algorithm has been applied on a pixel-by-pixel basis to the ~6700 SeaWiFS scenes, and the following outputs have been used: (1) The aerosol optical thickness at 865 nm, $\tau_{tot}(865)$, derived from the atmospheric signal at 865 nm through the multiple scattering inversion scheme

that was outlined above, (2) a flag set when absorption has been detected at 510 nm, and (3) the Ångstrøm exponent computed between 443 and 865 nm, $\alpha(443,865)$, which has been preferred to the commonly used near infrared exponent because it is sensitive to absorption:

$$\alpha(443, 865) = -\frac{\log[\tau_{tot}(443)/\tau_{tot}(865)]}{\log[443/865]} \qquad (2)$$

[28] These three quantities have been binned into a rectangular grid of 0.1° latitude and longitude resolution, to create monthly, seasonal, and annual composites, either for each individual year or for a "climatological" period where all 7 years are pooled together. Observations contaminated by sun glint or turbid Case 2 waters are removed from the binning process. Pixels identified as dusty are reset to maritime aerosols when their number is lower than half the number of valid pixels in a moving 3-by-3 pixel box. This filtering aims at removing isolated bright pixels that are essentially due to unidentified clouds or cloud borders.

[29] Concerning the optical thickness and Ångstrøm exponent, the average quantity in each bin is derived as a simple arithmetic mean. Two average values are derived for the optical thickness. The first one, $\tau_{tot}(865)$, is computed whatever the selected aerosol type, whereas the second one is computed only for the pixels where dust has been detected, and after removal of the constant backgrounds of maritime, continental and H_2SO_4 aerosols (corresponding to an optical thickness of 0.06 at 865 nm); it will be referred to as τ_{dust}. For a given area, the mean optical thickness of dust plumes is obtained by averaging τ_{dust} over the total number of dust pixels (in that case, by definition $\tau_{dust} \geq \tau_{tot}$). On the contrary, the overall contribution of dust over the same area is obtained by averaging τ_{dust} over all pixels, whatever their classification (dusty or clear).

[30] For a given period of time, the frequency of dust detection, which will be referred to as f_{dust} (expressed as a percentage), is computed from the ratio of the number of clear-sky pixels for which the dust flag was raised to the total number of clear-sky pixels over the same period. The dust occurrence has been also examined in terms of the absolute number of detection events, which will be referred to as N_{dust}. The use of f_{dust} is adapted to the case of climatological composites for which the number of observations is large and similar among the different situations under examination, whereas the use of N_{dust} is necessary when examining month-to-month evolutions with a greatly fluctuating number of observations due to changes of the cloud coverage.

[31] The number of nonglint, clear-sky observations summed up for each season and over the 1998-to-2004 time period is provided in Figure 2. As expected, winter is the season with the smallest density of observations because cloudiness is high. Surprisingly, more valid observations are obtained in fall as compared to summer (especially in the Levantine basin), which is somewhat the opposite of usual expectations. This is not due to cloudiness, which is lower in summer than in fall over the whole Mediterranean Sea, but is actually due to the higher occurrence and extent of sun glint in summer. At this season, Sun glint leads to the elimination of ten times more pixels than in fall, which is

Table 1. Characteristics of the AERONET-SeaWiFS Matchup Data Set

Site Name	Location	Years[a]	N AERONET[b]	N SeaWiFS[c]	N Matchups[d]
Villefranche sur mer	43.684°N, 7.329°E French Riviera	2004	235	105	76
IMC Oristano	39.91°N, 8.5°E West coast of Sardinia	2000–2003	934	316	84
Venise	45.3142°N, 12.508°E Off the Venice lagoon	1999–2004	1261	274	159
Lampedusa	35.517°N, 12.632°E South of Sicily	2000, 2003, 2004	383	70	42
Forth Crete	35.333°N, 25.282°E North coast of Crete	2003, 2004	532	192	134
Erdemli	36.565°N, 34.255°E South coast of Turkey	2000, 2001 2003, 2004	909	172	64
All sites			4254	1129	559

[a]The years for which Level-2 AERONET data are available.
[b]Total number of days with Level-2 AERONET data.
[c]The total number of AERONET-SeaWiFS matchups, after Sun glint and Case 2 waters have been excluded.
[d]The total number of valid AERONET-SeaWiFS matchups, after rejection criteria have been applied (see text).

overcompensating for the potentially higher number of observations due to a low cloudiness.

## 3. Results

3.1. Comparison With AERONET

[32] Before discussing the distributions and temporal changes of the aerosol optical thickness and aerosol types, a validation is presented for $\tau_{tot}(865)$ and $\alpha(443,865)$ based on Level-2, cloud-screened and quality-controlled data from six coastal sites of the AERONET [*Holben et al.*, 1998; *Dubovik et al.*, 2000], providing a sampling in the western, central, and eastern Mediterranean (see Table 1 and Figure 3).

[33] The procedure to generate matchup points is as follows: a 3 by 3 pixel box is extracted from the daily maps of optical thickness, centered on the marine area the closest of the exact site location. The shift is of one or two
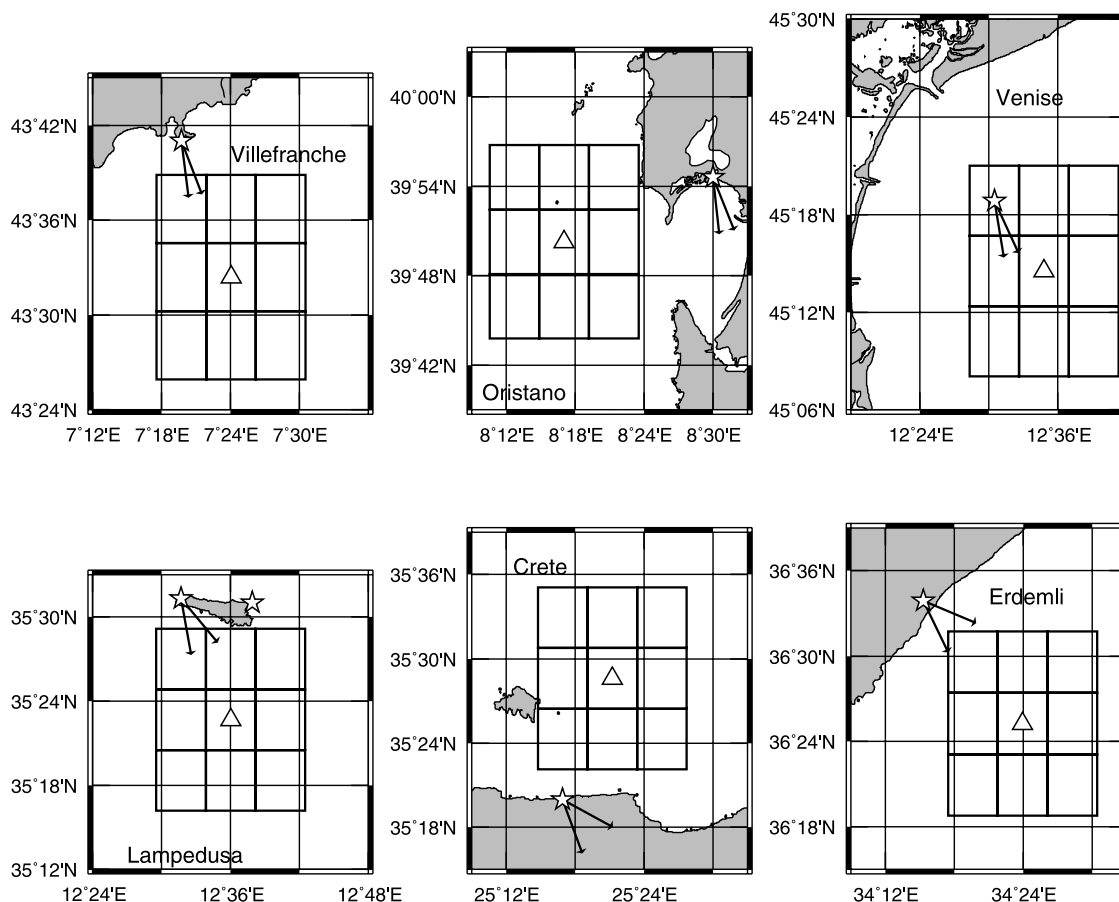
Figure 3. Location of the six AERONET sites (stars) selected for the validation of $\tau_{tot}(865)$ and $\alpha(443,865)$ (sea also the red stars in Figure 5a and Table 1). The position of the 3 by 3 SeaWiFS pixel box used for the matchup with the AERONET data is indicated (triangle at the center), as well as the azimuth of the sun at the time of the satellite pass (two arrows; one is for 21 June and the other one for 21 December).
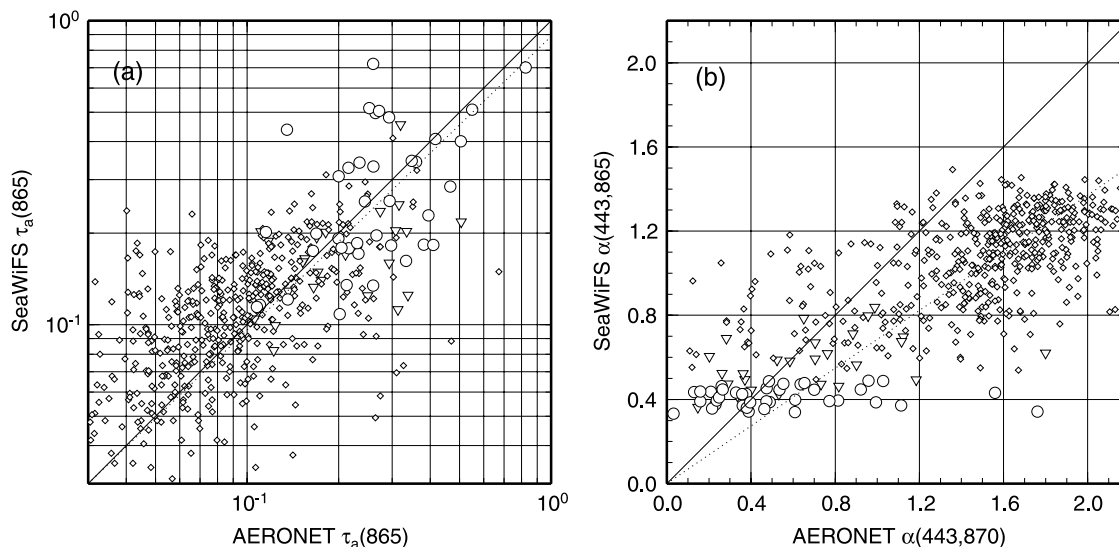
Figure 4. Comparison of (a) $\tau_{tot}(865)$ and (b) $\alpha(443,865)$, derived either from the AERONET or from the application of the algorithm to SeaWiFS. The rationale for producing this set of matchup points is explained in section 3.1 (see also Table 1). Diamonds are for nonabsorbing aerosols (i.e., the 3×3 pixels of the SeaWiFS images were all identified by the algorithm as nonabsorbing aerosols), circles are for dust atmospheres (all pixels identified as absorbing aerosols), and inverted triangles are for a mix of both types of aerosols. The solid line is the 1:1 line, and the dotted line is a simple linear fit with the intercept forced to zero.

(three in one case) SeaWiFS GAC pixels (Figure 3), in order to be sufficiently far away from the coast so that contamination either by the environment effect on the satellite radiance (bright land) or from Case 2 turbid waters is avoided. When the photometer is installed on a coastline oriented toward south, the 3-by-3 pixel area was also selected so as to be optimally placed with respect to the orientation of the Sun photometers when they took measurements at the time of the SeaWiFS pass (as indicated by the arrows in Figure 3).

[34] The group of nine pixels is rejected from the analysis as soon as one pixel is classified as cloud or glint or turbid Case 2 water, when the solar zenith angle is larger than 70 degrees, as well as when the standard deviation within the box is larger than 0.065 for $\tau_{tot}(865)$ or $\tau_{tot}(443)$ or larger than 0.2 for $\alpha(443,865)$. These thresholds were empirically determined in order to eliminate approximately 10% of the data with the highest standard deviations. Finally, situations where pixels are identified as absorbing aerosols, whereas the AERONET $\tau_{tot}(865)$ is lower than 0.1, which is the limit of detection of the algorithm [see *Nobileau and Antoine*, 2005], are considered as erroneous detections of absorbing aerosols and are removed from the validation exercise.

[35] The AERONET data are similarly screened in order to eliminate dubious data or unstable conditions, which are both undesirable when performing a validation exercise. Therefore data are not further considered when either $\alpha(443,865)$ is negative or the absolute value of the difference between $\alpha(443,865)$ and $\alpha(675,865)$ is larger than 0.4 or finally when the standard deviation of $\tau_{tot}(865)$ is larger than 0.065 within a time window of ±1 hour around the SeaWiFS overpass.

[36] When all criteria are satisfied, average quantities are computed on the one hand over the nine SeaWiFS pixels

and, on the other hand, over all AERONET observations found within ±15 min of the SeaWiFS overpass. A total of 559 matchup points have passed all criteria (see Table 1), 37 being in winter (DJF), 104 in spring, 291 in summer, and 127 in fall.

[37] The results of the comparison are satisfactory for $\tau_{tot}(865)$ (Figure 4a), with a regression slope close to 1 (= 0.89, with a correlation coefficient, r^2, of 0.78). These numbers would not significantly improve by removing matchup points for which $\tau_{tot}(865) < 0.05$, as was done by *Jamet et al.* [2004] in order to remove obvious outliers. When only the dust pixels are considered (65 points), the slope is 0.88 and the correlation coefficient is 0.80. The dispersion of the points is important, albeit not larger than usually observed in such validation exercises [*Santoleri et al.*, 2002; *Jamet et al.*, 2004; *Wang et al.*, 2005]. This validation, which includes high optical thicknesses, qualifies the inversion scheme and allows $\tau_{tot}(865)$ to be quantitatively discussed.

[38] The results are not so good for $\alpha(443,865)$ (Figure 4b), with a regression slope of only 0.69 (yet $r^2 = 0.94$). The overall underestimation of the SeaWiFS-derived Ångstrøm exponents, as compared to AERONET values, has already been identified by other, similar, validation exercises performed over the Mediterranean Sea [e.g., *Santoleri et al.*, 2002; *Jamet et al.*, 2004]. It is essentially explained by the characteristics of the 12 aerosol models considered in the first pass of atmospheric correction (cf. section 2), with ceiling values of the Ångstrøm exponents at ~1.5, whereas the AERONET provides values up to ~2.2. These large exponents cannot be reproduced without a modification of the set of aerosol models, for instance by using Jünge models as in the work of *Jamet et al.* [2004]. This underestimation of $\alpha(443,865)$ implies that this exponent has to be discussed
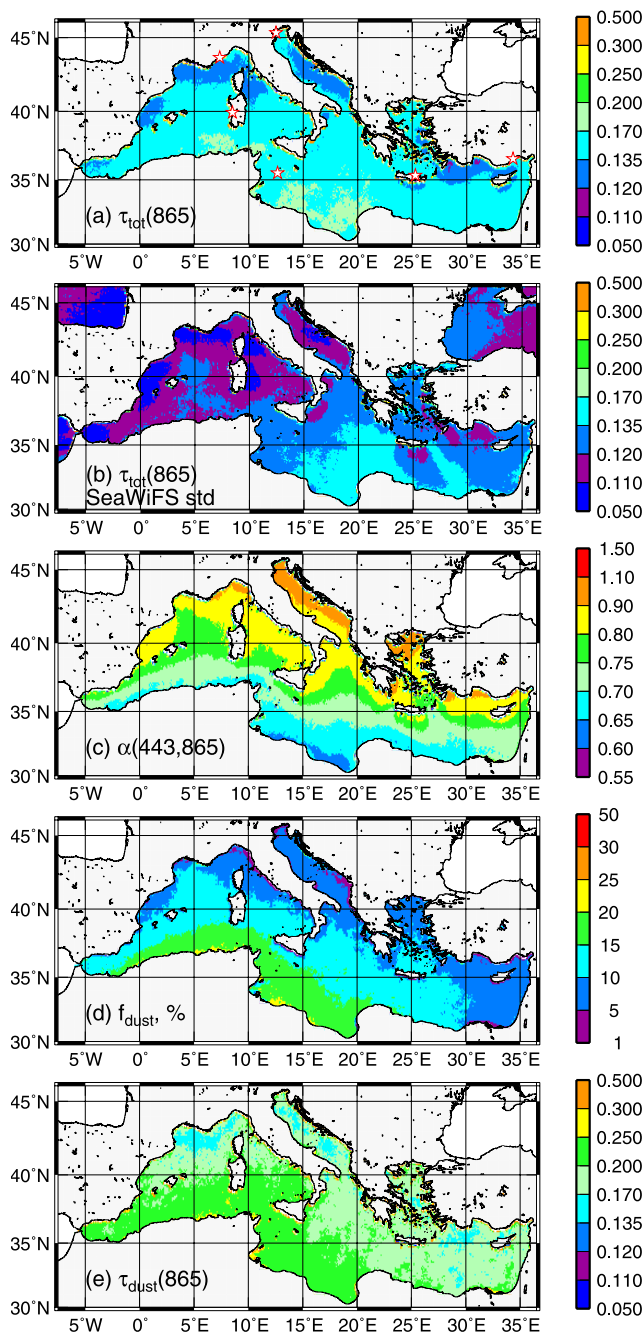
Figure 5. The 7-year (1998–2004) climatological averages of (a) $\tau_{tot}(865)$, (b) the same quantity as obtained from the NASA standard SeaWiFS products, (c) $\alpha(443,865)$, (d) f_{dust}, and (e) $\tau_{dust}(865)$. The red stars in Figure 5a are the six AERONET sites selected for validation (Figures 3 and 4).

only in a relative sense, i.e., only in terms of spatial distributions and temporal evolutions.

3.2. Climatological (1998–2004) Picture

[39] The 7-year average of the total aerosol optical thickness at 865 nm is of about 0.17 (Figure 5a), which is larger than the dust-free, open ocean values typically reported, for instance above the Pacific and Atlantic

[*Villevalde et al.*, 1994] or in Hawaii [*Dubovik et al.*, 2002]. This larger aerosol load, which is due to the surrounding of the basin by land masses, is consistent with previous determinations, as derived for instance from the Meteosat [*Moulin et al.*, 1998] or the SeaWiFS [*Jamet et al.*, 2004] observations. The well-known north-south gradient clearly appears, with, on the average, the clearest areas ($\tau_{tot}(865) \sim 0.125$) in the northernmost part of the western Mediterranean, the central Adriatic Sea, and the southern coasts of Turkey, whereas the south Ionian Sea, off Libya, shows the highest optical thickness ($\sim$0.2). The same overall organization appears in the NASA standard SeaWiFS products (Figure 5b), with lower values, however. This difference is likely due to the severe elimination of bright pixels in the NASA algorithms, which use a threshold of 0.027 on the total reflectance at 865 nm, eliminating therefore all moderately to highly thick dust plumes from further processing. When the algorithm proposed here is run with this low near infrared threshold for cloud elimination and without any use of the dust models (i.e., using only the 12 Shettle and Fenn models), the same average value is obtained for the optical thickness. The standard SeaWiFS product is therefore closer to a clear-sky maritime aerosol optical thickness, while the optical thickness produced here includes more turbid atmospheres as well.

[40] The distribution of $\alpha(443,865)$ (Figure 5c) nearly mirrors the distribution of $\tau_{tot}(865)$, with high exponents along the coasts of Europe and low exponents along the coasts of Africa. The association of high optical thicknesses with low exponents is the footprint of Saharan dust, which is characterized by low Ångstrøm exponents due to a high proportion of large particles and to absorption in the blue. Large exponents are conversely typical of small particles, usually nonabsorbing small continental aerosols or pollution aerosols. These two types of aerosols are mostly originating from the European continent and its urbanized areas, which explain the observed distribution. It is worth noting, however, that the progressive settling of the largest dust particles along the Africa-to-Europe transport also leads to a progressive increase of the Ångstrøm exponents. In spite of the well-known Saharan dust contamination of the Mediterranean atmosphere, very low $\alpha(443,865)$ values are not observed, which indicates the presence of permanent backgrounds of smallest particles of continental origin.

[41] The role of Saharan dust in shaping the distribution of $\tau_{tot}(865)$ and $\alpha(443,865)$ is confirmed by the f_{dust} distribution (Figure 5d), which again follows the same organization, except in the south Levantine basin where it remains on average <10% (but recall that this is the climatological average over 7 years). The mean optical thickness of dust plumes, τ_{dust} (Figure 5e), which is never lower than 0.2, again respects the same north-south organization, although large values (>0.25–0.3) are more homogeneously distributed than for the other parameters. This result only means that the average optical thickness of the dust plumes is, on this climatological representation, similar whatever the area.

3.3. Mean (1998–2004) Seasonal Variability

[42] The climatological (1998–2004) seasonal maps of τ_{tot}, $\alpha(443,865)$, f_{dust}, and τ_{dust} are displayed in Figure 6. The total optical thickness (panels on the left) shows a
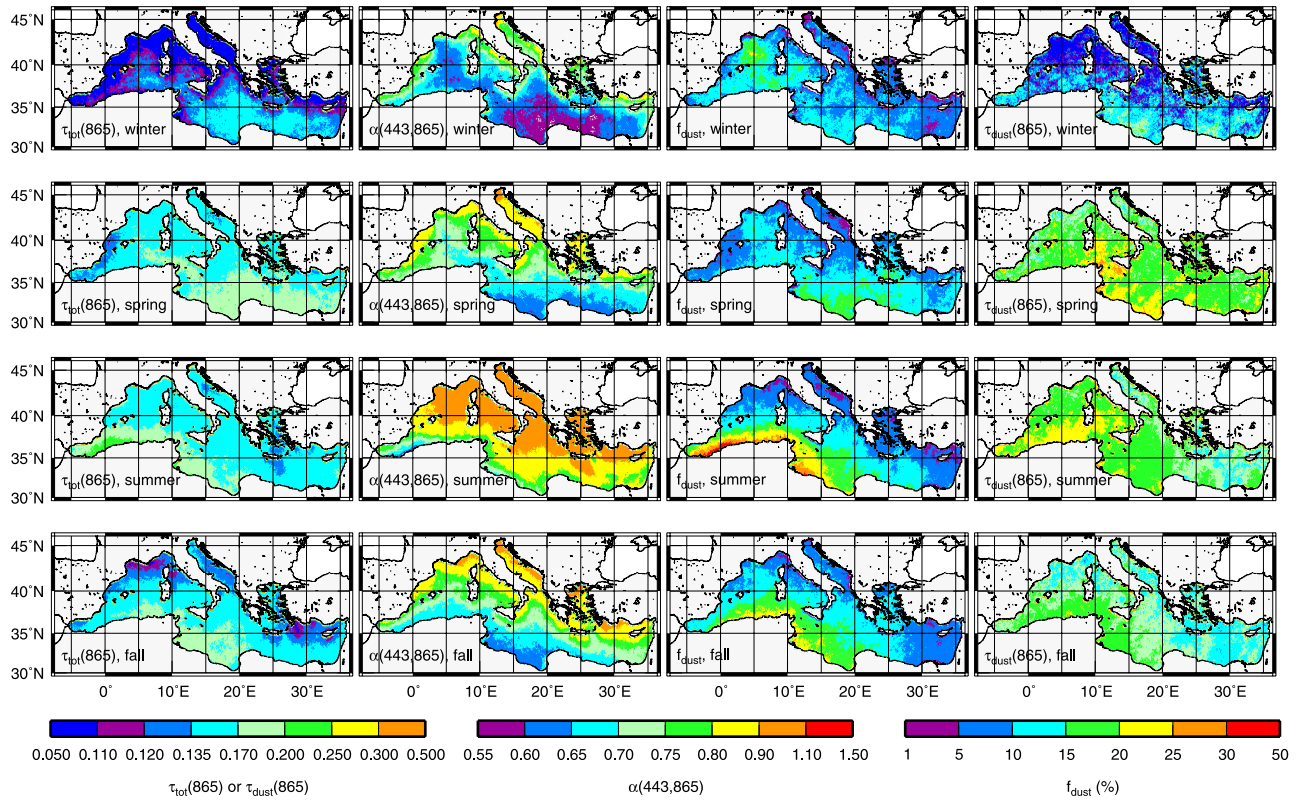
Figure 6. The 7-year (1998–2004) climatological seasonal averages of $\tau_{tot}(865)$ (left column), $\alpha(443,865)$ (second column from the left), (c) f_{dust} (second column from the right), and (d) $\tau_{dust}(865)$ (right column).

marked seasonality, with minimum values in winter, <0.125 in the western basin and <0.15 in the eastern part. During spring, the optical thickness first increases in the south eastern Mediterranean (<35°N) and to a lower extent in the western part. The converse situation prevails in summer, with maximum $\tau_{tot}(865)$ in the southwest and south Ionian (about 0.25), whereas the south Levantine goes back to much clearer atmospheres ($\tau_{tot}(865) < 0.15$), especially south of Crete.

[43] Again, the distribution of $\alpha(443,865)$ (Figure 6, second column from the left) closely matches that of $\tau_{tot}(865)$, with the coupling already observed between high optical thicknesses and low exponents. The highest exponents are found in summer in the northern half of the Mediterranean.

[44] The seasonal cycle of f_{dust} (Figure 6, second column from the right) exhibits a distinct maximum in summer, with values >20% along the coasts of Africa. The same patterns appear in fall, with, however, f_{dust} on average 10% lower than in summer. The minimum of dust occurrence is clearly in winter, except in the northwestern basin, where a distinct spot of relatively high of f_{dust} is observed between the Balearic Islands and Corsica. This spot still exists in spring, with lower values, however. During spring, the maximum of f_{dust} is located in the Ionian and Levantine basins, with moderate values (<20%).

[45] If the maximum occurrence of dust is definitely found in summer, it does not seem to be associated to

denser aerosol plumes. Indeed, the mean optical thickness of these plumes, τ_{dust} (Figure 6, column on the right), is about the same in spring and summer (i.e., ~0.3), and is even larger in spring in the eastern part. At the end, the mean optical thickness is similar in spring and summer, whereas the dust transport is probably much larger in summer (because f_{dust} is higher), in terms of mass of particles.

[46] The present SeaWiFS-based climatological description of the seasonality of aerosol loads over the Mediterranean is consistent with the analysis of the 11 years (1983–1994) of daily Meteosat images by *Moulin et al.* [1998], except for the significant dust transport that is revealed here in fall and which was not previously detected. Whether this difference is of methodological order or reveals a change in dust transport between the two study periods cannot be resolved here.

[47] The data that were pooled together to produce the maps in Figure 6 have been also used to generate climatological seasonal cycles over the three main regions of the Mediterranean Sea (Figure 7). These three regions are used on the one hand because they correspond to the three main pathways of the dust transport from Africa to Europe [e.g., *Alpert et al.*, 1990], and, on the other hand, in order to allow comparison with previous studies that already used this subdivision [*Moulin et al.*, 1998]. They are of similar extent, with areas of 1.07, 0.76 and 0.86 × 10^6 km^2 for the western, central, and eastern basins, respectively.
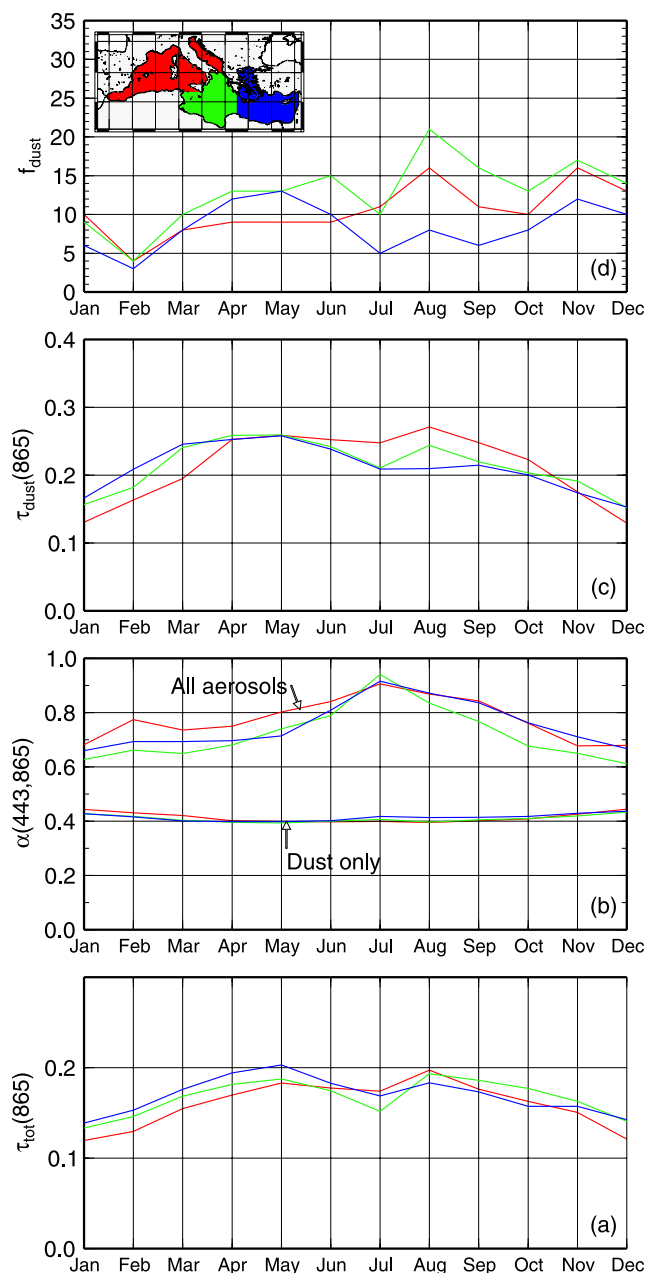
Figure 7. The 7-year (1998–2004) climatological seasonal cycles of (a) $\tau_{tot}(865)$, (b) $\alpha(443,865)$ for all aerosols or when only dust is considered, (c) $\tau_{dust}(865)$, and (d) f_{dust}. The red, green, and blue curves are for the western, central, and eastern Mediterranean basins, respectively. The delineation of the three basins is shown in insert.

[48] Very similar cycles are shown for $\tau_{tot}(865)$ in the three basins (Figure 7a), with minimum values in winter, two relative maxima in May and August, and a relative minimum in July (the latter being not obvious for the western basin). The eastern basin has the highest $\tau_{tot}(865)$ from December to June, and the minimum is usually in the western basin. Surprisingly, the same cycle does not show up for $\alpha(443,865)$ (Figure 7b), which has maxima in July–September for all three basins. This average cycle is actually strongly shaped by the large $\alpha(443,865)$ values in summer

along the northern coasts of the basins. Conversely, when the same exponent is computed for only those pixels that were identified as dusty, a nearly constant value of 0.4 is found. This value is simply characteristic of the *Moulin et al.* [2001a] dust models.

[49] The average cycle of the mean optical thickness of dust plumes, τ_{dust} (Figure 7c), is similar to that of the total optical thickness, except for the first relative maximum, which occurs in April instead of May. The largest differences among the three basins are observed in the f_{dust} cycles, with the central Mediterranean clearly showing the highest dust occurrences in summer and fall.

[50] The information displayed in Figures 6 and 7 are summarized in Table 2, as the seasonal averages of τ_{tot}, τ_{dust}, f_{dust}, and N_{dust} over the three subbasins. The maximum of f_{dust} is clearly in spring and fall in the eastern part and in summer and fall in the central and western parts. A relative maximum (10%) occurs in winter in the western basin. When looking at the absolute number of pixels identified as dusty (N_{dust}), the maximum is in fall in each basin. Looking successively at each season, the maximum of τ_{dust} clearly moves from the eastern to the central and the western basins, from winter to spring and to summer and fall, respectively. The overall maximum is in spring for the central and eastern seas. The three lower values are for the winter. A similar change occurs for the total optical thickness, except in fall when the maximum is in the central Mediterranean.

[51] Considering the method used by *Moulin et al.* [1998] to derive from METEOSAT what they called "average optical depth due to dust," the values in Table 2 to be compared to the values in their Table 1 are the τ_{tot} to which the constant backgrounds of tropospheric and stratospheric aerosols are removed, and then transferred to 550 nm using a mean exponent of 0.6. After this transformation, the values derived here from SeaWiFS are usually larger than those derived by *Moulin et al.* [1998] from METEOSAT, by as much as 80% (eastern basin in winter and fall; western basin in fall) and often by more than 25%. The SeaWiFS values are lower than the METEOSAT values only in the central basin in summer (−18%), and nearly equal (3%) in the same area in spring. Although part of these increases might be attributable to methodological differences between these two studies, they are large enough to indicate that the transport of dust aerosols over the Mediterranean is more intense during the time period investigated here as compared to the early 1990s examined in the study by *Moulin et al.* [1998].

3.4. Aerosol Models

[52] The dust optical thickness is dependent on the aerosol model that is eventually selected during the atmospheric correction. Relatively few models have been proposed, and the 18 models recently published by *Moulin et al.* [2001a] have been adopted here. It is therefore timely to examine how frequently each of the 18 models has been used. The model names are starting with either "BDS," corresponding to the refractive index of *Patterson* [1981] or with "BDW" for another refractive index leading to a lower absorption in the blue. The first number (1, 2, or 3) following the three-letter denomination refers to the size distribution, with a higher proportion of large particles for

Table 2. Climatological (1998–2004) Seasonal Averages of $\tau_{tot}(865)$, $\tau_{dust}(865)$, f_{dust}, and N_{dust} for the Western, Central, and Eastern Mediterranean

	$\tau(865)$			$\tau_{dust}(865)$			f_{dust}, %			N_{dust} (10^6 pixels)		
	Western	Central	Eastern	Western	Central	Eastern	Western	Central	Eastern	Western	Central	Eastern
Winter (DJF)	0.120	0.136	0.143	0.129	0.150	0.162	10	9	7	0.622	0.395	0.332
Spring (MAM)	0.170	0.179	0.192	0.237	0.254	0.253	8	12	11	0.794	0.744	0.729
Summer (JJA)	0.184	0.175	0.179	0.260	0.236	0.221	12	16	8	1.369	1.064	0.563
Fall (SON)	0.160	0.173	0.161	0.208	0.202	0.189	12	16	9	0.424	1.376	0.960

"3" than for "2" than for "1." The second number (2, 5, or 7) refers to the vertical repartition of the aerosol, which is homogeneously distributed from the surface to either 2, 5, or 7 km.

[53] Statistics of the aerosol model selections are provided in Table 3. They show that the BDW family of aerosols is selected in ~80% of the cases (up to 90% in summer and 60% in winter), and that among this family, the BDW1 model is dominant (BDW2 and BDW3 suit only in 4% and 3% of the cases, respectively). This model is moderately absorbing and has a small proportion of large particles, hence a relatively steep spectral dependency for its scattering coefficient. When it is selected, the BDW1 model is combined with the two vertical distributions that are the most frequently used, i.e., the aerosol distributed from 0 to 7 km (~60%) or from 0 to 2 km (~30%). Overall, the second most frequently used aerosol model is the BDS1 (~15%), which is made of the same particle size distribution than the BDW1 but is more absorbing in the blue. In third position is the BDS3 model (~6% of all model selections). The BDS2 is the least used of all models.

[54] The most appropriate vertical distribution is when aerosols are from 0 to 7 km, and the second one is when aerosols are confined in the marine boundary layer (0–2 km). The intermediate case (0–5 km) is rarely selected. It is however difficult to assess whether this is representative of the true vertical distribution or sometimes results from compensating effects due to possible unrealistic vertical distributions combined with inappropriate optical properties.

[55] Overall, within the models proposed by *Moulin et al.* [2001a], the less absorbing models with the steeper spectral dependence of scattering are the most appropriate to describe the dust aerosol over the Mediterranean Sea. The reader is referred to Table 3 for a closer examination of the occurrence of each model as a function of the season and of its vertical distribution.

3.5. Interannual Variability of the Seasonal Patterns of the Dust Distribution

[56] The five parameters (τ_{tot}, $\alpha(443,865)$, f_{dust}, N_{dust}, and τ_{dust}), in spite of their specific features that were previously described, have similar average distributions and seasonal cycles. For this reason, and also because f_{dust} has shown the greatest seasonal and regional variability among the four parameters, this parameter only is considered for the analysis of the interannual variability. To support this analysis, seasonal maps of f_{dust} are separately displayed for each of the 7 years in Figure 8.

[57] Although winter is generally characterized by the lowest values of f_{dust} across the entire Mediterranean, the region between the Balearic Islands and Sardinia shows significant frequencies of dust aerosols in most years, especially from 2000 to 2004. Regional scale transport also occurs across the entire western Mediterranean in winter of 2001, and even over the whole Mediterranean in winters of 2003 and 2004. These two "anomalous" years are also characterized by large areas with mean Ångstrøm exponents below 0.5.

[58] Summer is confirmed as the season of maximum dust transport whatever the year, which is clearly revealed in Figure 8, with a band of large f_{dust} values along the African coast, from the Alboran Sea to the Ionian Sea.

Table 3. Statistics of the Dust Model Selections (See Text for the Meaning of the Model Names) in Terms of the Percentage of the Total Number of Pixels for Which Absorption Has Been Detected[a]

Winter		Spring		Summer		Fall		All Seasons	
BDW17	45.2	BDW17	37.8	BDW12	44.6	BDW17	48.6	BDW17	41.6
BDS17	19.8	BDW12	31.3	BDW17	34.1	BDW12	20.3	BDW12	26.1
BDS37	8.0	BDW15	5.8	BDW15	5.2	BDS17	8.8	BDS17	9.2
BDW12	6.4	BDS17	5.7	BDS17	3.8	BDS37	3.9	BDS37	4.2
BDS27	4.5	BDW27	4.3	BDW27	3.0	BDW15	3.7	BDW15	4.1
		BDS12	3.1			BDW27	3.1	BDW27	3.0
BDS	40.6		14.9		10.3		19.8		20.7
BDW	59.4		85.1		89.7		80.2		79.3
0–2 km	12.9		38.5		47.5		25.6		31.5
0–5 km	6.1		7.7		6.0		6.4		6.5
0–7 km	81.0		53.7		46.5		68.0		62.0

[a]The models that were selected in less than 3% of the situations are not shown. The "BDS" and "BDW" lines summarize the contribution of both families of dust aerosols, whatever the size distribution and the vertical repartition, and the last three lines summarize the contribution of the three different vertical distributions, whatever the aerosol model.
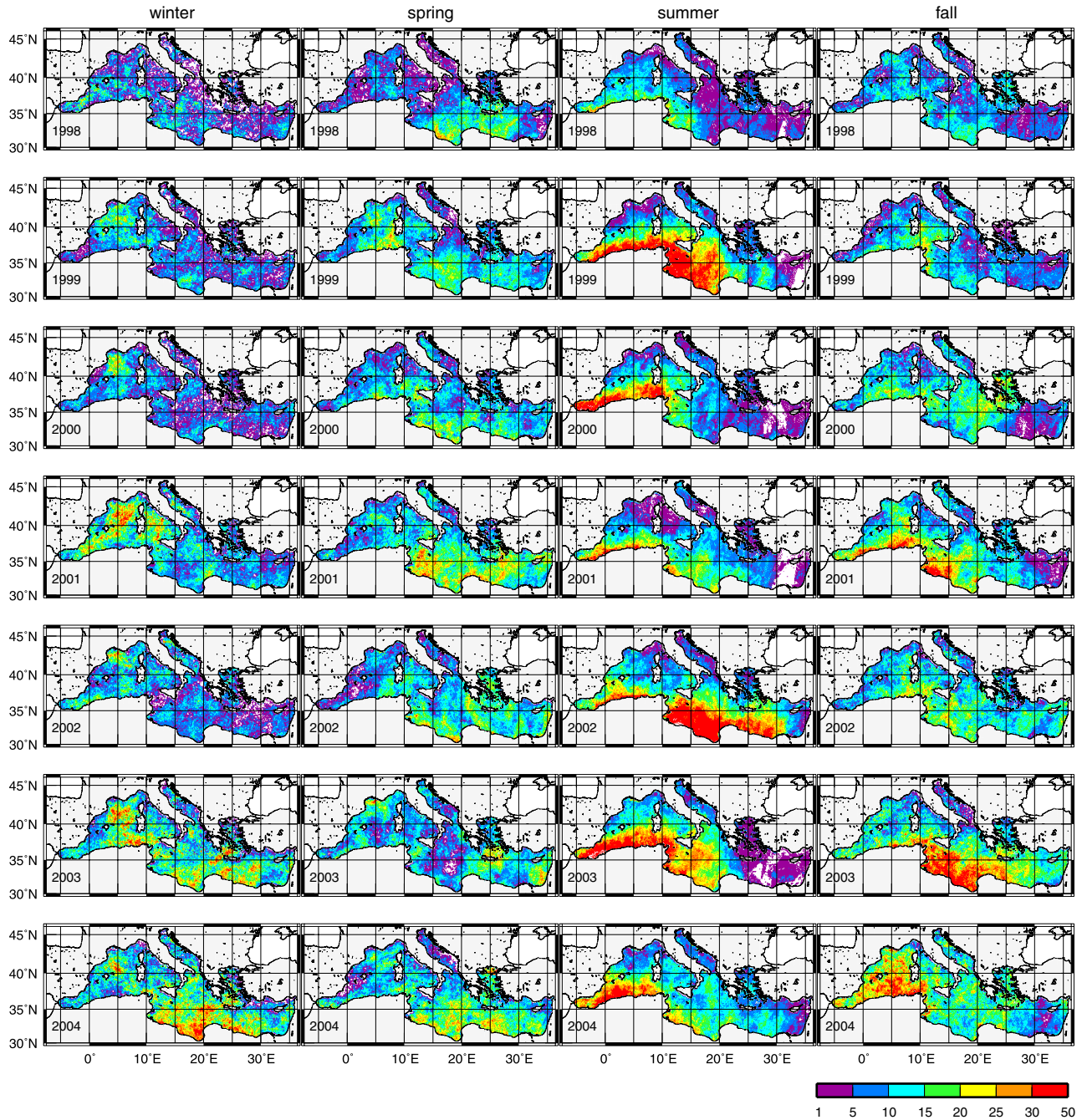
Figure 8. Seasonal occurrence of dust aerosols, f_{dust} (%), from 1998 (top) to 2004 (bottom).

[59] Spring and fall are showing the largest interannual changes. The area of maximum f_{dust} is nearly absent in fall of 1998, located between Sardinia, Sicily, and Tunisia in 1999, spread over a large band from the north of Algeria to Crete in 2000, concentrated along the Algerian, Tunisian, and Libyan coasts in 2001 (showing a ''summer-like pattern''), spread over a large part of the basin in 2002, concerning mostly the south Ionian Sea and south Levantine basin in 2003, and finally nearly restricted to the western basin in 2004. Very high f_{dust} (> 30%) are observed in falls of 2001, 2003, and 2004, whereas it generally does not exceed 25% at this season.

[60] Concerning spring, the maximum extent of dust was in 2001. For the other years, there is no clear organization, with areas of moderately high f_{dust} (about 20%) spread out over the different subbasins of the Mediterranean.

[61] These observations show that the interannual variability of the dust transport over the Mediterranean Sea does not show up as a slight modulation around a climatological and repeatable annual cycle. It is rather characterized by dramatic changes in the main pathways of atmospheric transport, resulting in highly contrasted situations. The only repeatable feature is the East-to-West shift of the transport from spring to summer and to fall, which has been previously described [*Moulin et al.*, 1998], and which can be
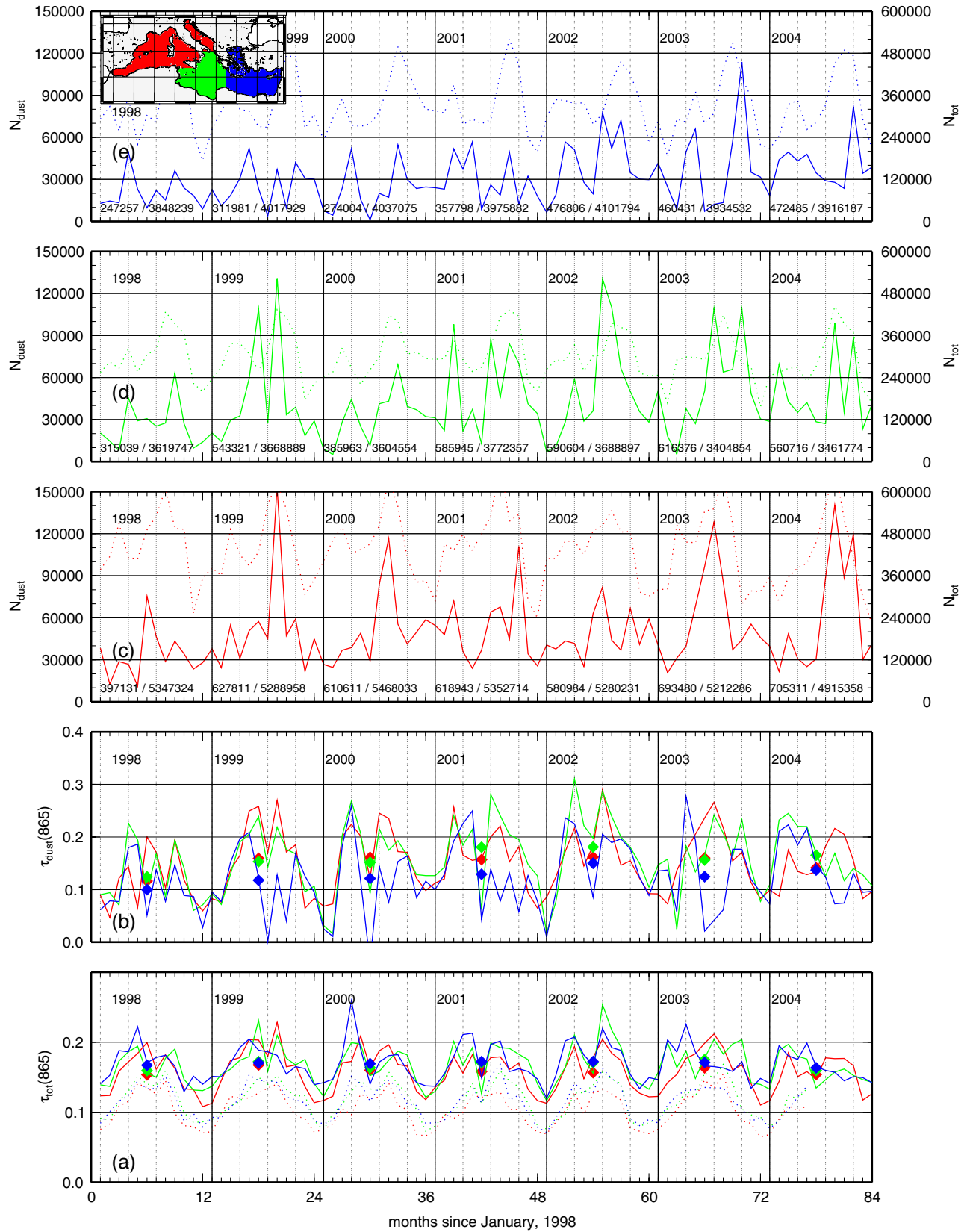
Figure 9

Table 4. Annual Averages of $\tau_{tot}(865)$ and $\tau_{dust}(865)$ for the Three Subbasins

	$\tau_{tot}(865)$			$\tau_{dust}(865)$		
	Western	Central	Eastern	Western	Central	Eastern
1998	0.153	0.159	0.167	0.116	0.124	0.100
1999	0.167	0.172	0.171	0.159	0.153	0.118
2000	0.160	0.163	0.169	0.161	0.152	0.121
2001	0.158	0.171	0.172	0.157	0.180	0.129
2002	0.157	0.171	0.172	0.162	0.181	0.150
2003	0.163	0.175	0.171	0.160	0.156	0.124
2004	0.154	0.160	0.163	0.141	0.165	0.137

mostly explained by the climatology of cyclonic circulations over the Mediterranean sea [*Alpert et al.*, 1990].

[62] The information provided in Figure 8 are summarized in Figure 9, as the 7-year, month-to-month, evolution of basin-average τ_{tot} (Figure 9a), τ_{dust} (Figure 9b), and N_{dust} in the western (Figure 9c), central (Figure 9d), and eastern (Figure 9e) Mediterranean.

[63] Concerning the total optical thickness (Figure 9a), the comments about the climatological cycle (Figure 7) remain grossly valid with a minimum in winter and relative maxima usually in spring or summer. The results obtained from the standard SeaWiFS products have been superimposed for comparison. The seasonal cycles are nearly identical when computed from the results of the standard SeaWiFS processing or from the present one, but the average values provided in the standard SeaWiFS products are lower by 38% on average. This difference disappears (not shown) when using the same technique for cloud elimination than in the standard SeaWiFS processing (as already mentioned for Figure 5). A recurrent feature is the seasonal westward shift of the dust transport, with the increase of optical thickness occurring one or two months later in the western Mediterranean than in the central and eastern basins. The central and eastern basins are actually where dust starts to become significant, sometimes as early as winter (for instance in 2003 and 2004).

[64] Concerning the dust optical thickness (Figure 9b), the seasonal evolution is similar to that of the total optical thickness, with however a larger range of values, from nearly zero in winter of 2001–2002 to a maximum of about 0.3 in spring of 2002. The annual averages (diamonds on Figure 9b; values reported in Table 4) regularly increase from 1998 to 2002 and then remain nearly stable.

[65] Concerning N_{dust} (Figures 9c, 9d, and 9e), none of the three basins show a clear picture, with usually one or two, sometimes three, relative maxima occurring at various moments in the year. These seasonal evolutions show a considerable interannual variability, which is certainly driven

by the complex patterns of atmospheric circulation and rainfall over the Mediterranean and over the source regions. The seasonal cycles often markedly differ from the climatological picture previously described [e.g., *Moulin et al.*, 1998]. Although some recent changes may have occurred in the seasonal patterns of dust transport over the Mediterranean Sea, it is believed that these differences are partly due to the capability of the present algorithm to discriminate between absorbing and nonabsorbing aerosols, so that a dust-specific optical thickness can be derived, as compared to the algorithms using broadband visible METEOSAT observations that essentially assign the Rayleigh-corrected signal to dust aerosols for any pixel, after constant backgrounds of sulfate and H_2SO_4 aerosols have been removed. The other obvious feature appearing in Figures 9c, 9d, and 9e is an increase of N_{dust} over the study period. This evolution of the dust transport is now described.

3.6. General Evolution Over the 7-Year Study Period (1998 to 2004)

[66] The seasonal patterns and the year-to-year changes have been also quantified by computing in each basin the area that is frequently affected by dust plumes. For a given monthly composite and a given subbasin, this is obtained by summing up the area of all $0.1° \times 0.1°$ grid cells where $f_{dust} > 25\%$ (results on Figure 10). The value of 25% was arbitrarily chosen as representative of high dust loads. It has been checked that the seasonal patterns and the year-to-year changes are not appreciably modified for percentages between 15% and 30%. The impact of lowering (increasing) the threshold is essentially to shift the curves shown in Figure 10 toward larger (lower) values.

[67] The largest dust-contaminated areas are usually in the central Mediterranean (the smallest of the three subdivisions), where they can reach up to 65% of the basin area, whereas they concern a maximum of 25% and 45% of the basins for the eastern and western parts, respectively. Exceptions are for 2000 and 2004, where the largest areas are in the western Mediterranean. In 2000, this is due to a strong decrease in the dust transport toward the central basin (it is therefore a relative maximum), while in 2004 it is clearly due to the anomalously high dust content over the western basin in fall. The curves displayed in Figure 10 again illustrate the huge interannual variability in the dust occurrences, with annual cycles that would hardly be superimposed one on top of each other.

[68] The running averages in Figure 10 show a general increase of the dust occurrences from 1998 to 2004, in particular in the eastern Mediterranean. In this subbasin the average area where significant dust is detected is multiplied by nearly a factor of 5, which represents a change from ~3% to ~15% of the basin area. If the year 1998 is not

Figure 9. Seasonal cycles of (a) $\tau_{tot}(865)$ (the red, green, and blue solid curves are for the western, central, and eastern Mediterranean basins, respectively; the dotted curves are from the standard SeaWiFS products), (b) $\tau_{dust}(865)$, and (c, d, e) the absolute occurrence of dust aerosols, N_{dust}, for the western, central, and eastern Mediterranean, from 1998 to 2004. In Figures 9a and 9b, the diamonds are the annual averages (values reported in Table 4). In Figures 9c, 9d, and 9e the dotted curves are the total number of clear-sky pixels (scale on the right axis), and the two numbers given at the bottom of each panel and for each year are the total number of dusty pixels and the total number of pixels. The delineation of the three basins is shown in insert. The vertical bold lines indicate the month of January for each year, and the vertical dotted lines are for the months of April, July, and October.
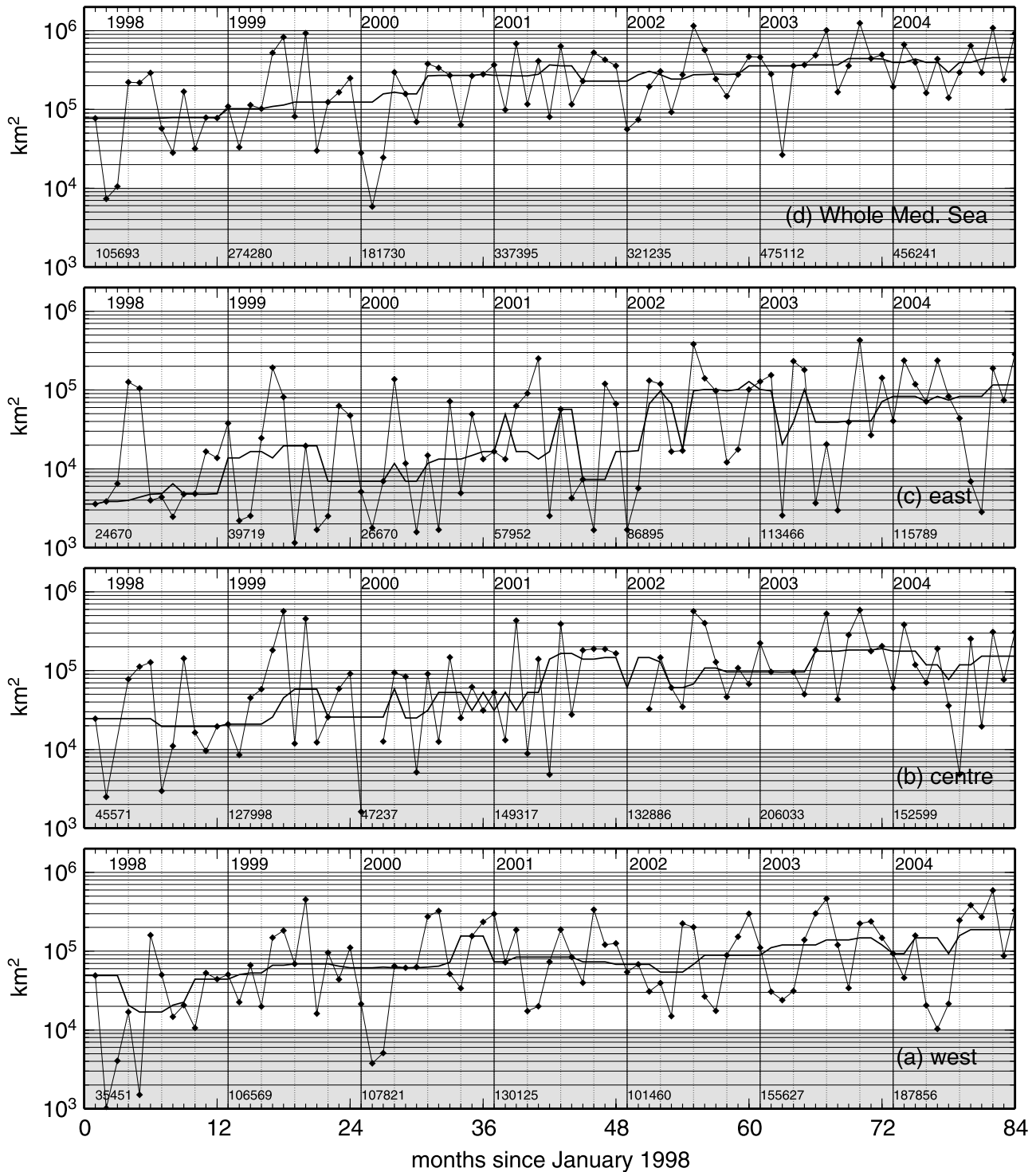
Figure 10. Month-to-month evolution, from 1998 to 2004, of the total area where $f_{dust} > 25\%$, for the (a) western, (b) central, (c) eastern, and (d) whole Mediterranean. The bold curve is a running average based on the monthly values (thin curve) and using a ±5 months window. The numbers given at the bottom of each panel and for each year are the mean of the monthly values (km^2). The vertical bold lines indicate the month of January for each year, and the vertical dotted lines are for the months of April, July, and October.

considered because it looks quite atypical with very low dust occurrences, the increase is still by a factor of ~3. Similar numbers are obtained for the western basin (factors of ~5 and ~2, from ~3% to ~15% of the basin area), whereas lower increases are observed in the central basin (~3 and ~1.5, i.e., from ~7% to ~20%). In the western and central basins, most of the increase occurs from 1998 to 2001, with a relative steadiness in the following years.
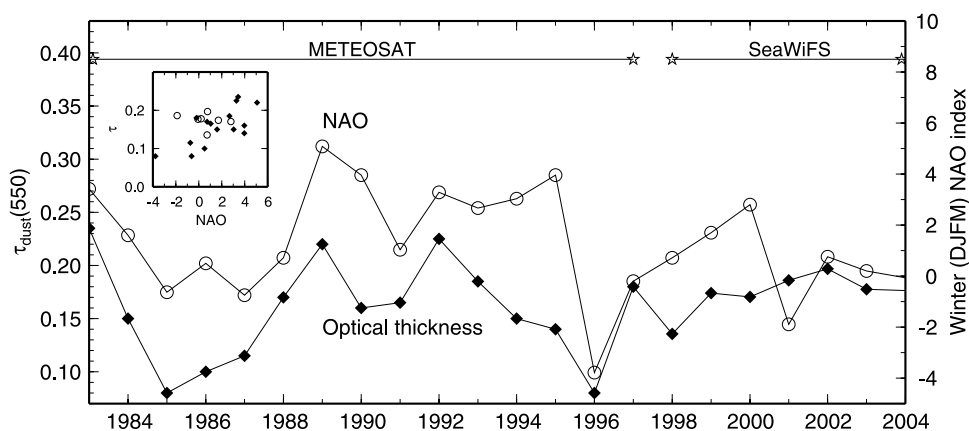
Figure 11. Time series of the North Atlantic Oscillation (NAO) winter index (scale on the right axis; open circles; data from http://www.cgd.ucar.edu/cas/jhurrell/Data/naodjfmindex.1864–2005.xls) and of the dust optical thickness (scale on the left axis; black diamonds). The values derived at 865 nm from the SeaWiFS data have been converted into values at 550 nm in order to be consistent with the results published by *Moulin et al.* [1997c] and *Moulin and Chiapello* [2004] (data courtesy C. Moulin). The transformation was performed with an Angstrom exponent of 0.4 (cf. Figure 7b). The inserted scatterplot of τ_{dust} versus the NAO includes the 15 points from the METEOSAT time series (black diamonds) and the seven points from the SeaWiFS time series (open circles).

[69] These evolutions are coherent with the average τ_{dust} values provided in Table 4, which are larger in 2004 than in 1998, by about 20%, 33%, and 37% in the western, central and eastern basins, respectively. The increase even reaches 50% between 1998 and 2002 (the year with maximum τ_{dust} everywhere) in the eastern basin. Because the dust transport looks really low in 1998, it is timely to also compute the percentages of change from 1999 to 2004. In that case, they become about −10%, 8%, and 16%. Therefore except for the western basin, the overall tendency is confirmed whatever the starting point used for the computation. It is worth noting that the changes displayed in Figure 10 somewhat overemphasize the increase over the study period, as compared to what can be seen when looking only at the average dust optical thickness (Figure 9b). The moderate increase observed in τ_{dust} actually occurs for levels close to the detection limit of the algorithm (optical thickness of about 0.15 at 865 nm), which explains the large increase of dust detection, with the optical thickness being more and more often above the detection threshold from the beginning to the end of the 7-year time series. This observation illustrates the sensitivity of the detection method.

[70] A number of processes may possibly be responsible for the observed increase in the dust optical thickness over the study period. They may include local changes in atmospheric circulation, local changes in rain rates and distribution, as well as modification of the dust mobilization from the source regions. A thorough examination of these local causes, which would require the corroborative study of several types of data over the same time period, is out of scope here. Another candidate has been examined, however, which is driven by atmospheric processes at larger scales, i.e., the change in the North Atlantic Oscillation (NAO) [e.g., *Hurrell*, 1995; *Hurrell et al.*, 2003]. This oscillation has already been identified as a driver of the decadal evolutions of the dust transport over the Mediterranean Sea and the North Atlantic [*Moulin et al.*, 1997c; *Moulin*

and Chiapello, 2004]. The 7-year τ_{dust} time series derived here from the SeaWiFS has been therefore appended to the 14-year time series previously derived from the METEO-SAT observations. The complete series has been plotted in parallel to the "winter NAO index," i.e., the average NAO index for the 4 months between December and March (Figure 11). The overall correlation between τ_{dust} and the winter index, which was first described by *Moulin et al.* [1997c], is confirmed for the SeaWiFS era, although the change in the NAO during this period is much less than during the METEOSAT era (from −2 to +3, as compared to −4 to +6). It is therefore legitimate to ascribe to the NAO the first-order changes observed here for τ_{dust} over the SeaWiFS era, whereas local and seasonal changes of τ_{dust} would stem from the processes briefly mentioned above (and possibly from other processes not identified here).

[71] To corroborate the trends observed here in f_{dust}, information about absorbing aerosols that might be provided by other remote sensing techniques have been sought for (other than simply the optical thickness). The most relevant parameter that was found is the Earth Probe-TOMS absorbing aerosol index [*Herman et al.*, 1997; *Torres et al.*, 1998], which is derived from measurements in the ultraviolet domain. Unfortunately, an unexplained wavelength-dependent calibration drift started after year 2000, which made these data unusable for a trend analysis (O. Torres, personal communication, 2005). The Ozone Monitoring Instrument (OMI) sensor on the AURA satellite [*Levelt et al.*, 2000] now provides the same index, yet only since October of 2004, which was useless to compare with the 7-year time series derived from SeaWiFS.

[72] Possible drawbacks in this temporal analysis might be produced on the one hand by a drift in the sensor calibration, which could bias the aerosol identification in the near infrared or the error budget at 510 nm, and, on the other hand, by a change in the average ocean reflectance at 510 nm. The first cause is unlikely however, since the

vicarious calibration of SeaWiFS has benefited from an outstanding effort that allowed maintaining the stability of the instrument. Concerning the ocean reflectance at 510 nm, there is not any indication of such a change.

[73] A modification in the balance between dry aerosol transport (the one accessible to the technique proposed here) and wet transport within clouds, which is by definition not seen by an inherently clear-sky method, might also lead to such an apparent increase of f_{dust}.

4. Conclusion

[74] A method was recently developed for the detection of blue-absorbing aerosols from ocean color satellite observations and was validated against in situ data [*Nobileau and Antoine*, 2005]. This method has been applied here to 7 years of observations from the SeaWiFS sensor, to describe the distribution of Saharan dust over the Mediterranean Sea, and to quantify the associated atmospheric burden. One objective was to conclusively demonstrate the applicability of the method when systematically used with large data sets and to validate more extensively its outputs by comparison with AERONET products.

[75] The general pictures that emerged from this work are consistent with the results from previous works, where the dust quantification over the Mediterranean Sea was performed either from broadband visible observations (i.e., METEOSAT) [*Moulin et al.*, 1998] or from other multichannel visible ocean color observations either from MODIS [*Barnaba and Gobbi*, 2004] or from SeaWiFS [*Jamet et al.*, 2004]. The seasonal cycle of the optical thickness is well captured in the three subbasins, with the lowest values in winter and the highest values in spring and summer. In addition, a strong interannual variability is observed, as well as an increasing trend in the dust transport during the study period. The main difference with previous works is the importance of the dust transport in fall, and higher dust optical thicknesses on the average.

[76] The method is therefore suitable to routinely map blue-absorbing aerosols over the ocean from the various ocean color sensor observations. It is for instance implemented into the operational processing chain for MERIS. It can advantageously complement the other techniques, in order to provide the most comprehensive as possible picture of aerosols over the ocean from various satellite platforms. These results also confirm that the sampling provided by SeaWiFS (i.e., a full coverage of the Mediterranean Sea within 2 days) is adapted to the study of aerosols.

[77] Improvements of the method are still desirable, however, in particular before it can be generalized to the global ocean. A first possibility is to progressively improve the knowledge of the global seasonal distribution of the marine reflectance at 510 nm, which would lead to an improvement of the detection capability (in other words, improving the uncertainty budget at 510 nm). This is reachable by permanently revising the global climatology for $\bar{\rho}_w(510)$ and $\sigma(\rho_w)$, by using the fleet of ocean color sensors presently in orbit, and also through blending of these data along with in situ determinations of the marine reflectance at 510 nm.

[78] The second improvement would be to introduce additional sets of dust aerosols specific to the other regions

of the planet where they are transported, i.e., mostly the Arabian Sea, the north Pacific and the seas around Australia. There is indeed a significant variability in the dust optical properties, in particular their single scattering albedo, among the different source regions [*Dubovik et al.*, 2002]. Introducing these differences would improve the retrieval of the aerosol optical thickness, in particular in the visible.

[79] Another step would be the introduction of additional external information or the use of additional spectral bands, in order to specifically determine whether the absorption detected at 510 nm is due to dust or to other absorbing aerosols such as soot or biomass burning aerosols. In the present work, however, this cannot have a strong impact on the results because the vast majority of absorbing aerosols over the Mediterranean Sea are of desert origin.

[80] These improvements would in turn improve the ocean color products themselves, such as the normalized water-leaving radiance, by improving the atmospheric correction process [e.g., *Moulin et al.*, 2001b].

References

Alpert, P., B. Neeman, and Y. Shay-El (1990), Intermonthly variability of cyclone tracks in the mediterranean, *J. Clim.*, 3, 1474–1478.

Andreae, M. O. (1996), Raising dust in the greenhouse, *Nature*, 380, 389–390.

Antoine, D., and A. Morel (1999), A multiple scattering algorithm for atmospheric correction of remotely sensed ocean colour (MERIS instrument): principle and implementation for atmospheres carrying various aerosols including absorbing ones, *Int. J. Remote Sens.*, 20, 1875–1916.

Barnaba, F., and G. P. Gobbi (2004), Aerosol seasonal variability over the Mediterranean region and relative impact of maritime, continental and Saharan dust particles over the basin from MODIS data in the year 2001, *Atmos. Chem. Phys. Discuss.*, 4, 4285–4337.

Barnes, R. A., R. E. Eplee Jr., G. M. Schmidt, F. S. Patt, and C. R. McClain (2001), Calibration of SeaWiFS. I. Direct techniques, *Appl. Opt.*, 40, 6700–6882.

Bellouin, N., O. Boucher, D. Tanré, and O. Dubovik (2003), Aerosol absorption over the clear-sky oceans deduced from POLDER-1 and AERONET observations, *Geophys. Res. Lett.*, 30(14), 1748, doi:10.1029/2003GL017121.

Boucher, O., and D. Tanré (2000), Estimation of the aerosol perturbation to the Earth's radiative budget over oceans using POLDER satellite aerosol retrievals, *Geophys. Res. Lett.*, 27, 1103–1106.

Bricaud, A., and A. Morel (1987), Atmospheric corrections and interpretation of marine radiances in CZCS imagery: use of a reflectance model, *Oceanol. Acta*, SP-7, 33–50.

Brooks, N., and M. Legrand (2000), Dust variability over northern Africa and rainfall in the sahel, in *Linking Climate Change to Land Surface Change*, edited by S. J. McLaren and D. Kniveton, pp. 1–25. Springer, New York.

Charlson, R. J., S. E. Schwartz, J. M. Hales, R. D. Cess, J. A. Coakley, J. E. Hansen, and D. J. Hoffman (1992), Climate forcing by anthropogenic aerosols, *Science*, 255, 423–430.

Chiapello, I., and C. Moulin (2002), TOMS and METEOSAT satellite records of the variability of Saharan dust transport over the Atlantic during the last two decades (1979–1997), *Geophys. Res. Lett.*, 29(8), 1176, doi:10.1029/2001GL013767.

Chiapello, I., P. Goloub, D. Tanré, J. Herman, O. Torres, and A. Marchand (2000), Aerosol detection by TOMS and POLDER over oceanic regions, *J. Geophys. Res.*, 105, 7133–714.

Clarke, G. L., G. C. Ewing, and C. J. Lorenzen (1970), Spectra of backscattered light from the sea obtained from aircraft as a measure of chlorophyll concentration, *Science*, 167, 1119–1121.

Deuzé, J. L., M. Herman, P. Goloub, D. Tanré, and A. Marchand (1999), Characterization of aerosols over ocean from POLDER/ADEOS-1, *Geophys. Res. Lett.*, 26, 1421–1424.

Deuzé, J.-L., P. Goloub, M. Herman, A. Marchand, G. Perry, D. Tanré, and S. Susana (2000), Estimate of the aerosols properties over the ocean with POLDER, *J. Geophys. Res.*, 105, 15,329–15,346.

Donaghay, P. L., P. S. Liss, R. A. Duce, D. R. Kester, A. K. Hanson, T. Villareal, N. W. Tindale, and D. J. Gifford (1991), The role of episodic atmospheric nutrient inputs in the chemical and biological ecosystems, *Oceanography*, 4, 62–70.

Dubovik, O., A. Smirnov, B. N. Holben, M. D. King, Y. J. Kaufman, T. F. Eck, and I. Slutsker (2000), Accuracy assessments of aerosol optical properties retrieved from Aerosol Robotic Network (AERONET) sun and sky radiance measurements, *J. Geophys. Res.*, 105, 9791–9806.

Dubovik, O., B. N. Holben, T. F. Eck, A. V. Smirnov, Y. J. Kaufman, M. D. King, D. Tanré, and I. Slutsker (2002), Variability of absorption and optical properties of key aerosol types observed in worldwide location, *J. Atmos. Sci.*, 59, 590–608.

Duce, R. A., et al. (1991), The atmospheric input of trace species to the World ocean, *Global Biogeochem. Cycles*, 5, 193–259.

Fu, G., K. S. Baith, and C. R. McClain (1998), SeaDAS: The SeaWiFS Data Analysis System, paper presented at 4th Pacific Ocean Remote Sensing Conference, Qingdao, China.

Gordon, H. R. (1978), Removal of atmospheric effects from satellite imagery of the oceans, *Appl. Opt.*, 17, 1631–1636.

Gordon, H. R. (1990), Radiometric considerations for ocean color remote sensors, *Appl. Opt.*, 29, 3228–3236.

Gordon, H. R. (1997), Atmospheric correction of ocean color imagery in the Earth Observing System era, *J. Geophys. Res.*, 102, 17,081–17,106.

Gordon, H. R., and M. Wang (1994a), Retrieval of water-leaving reflectance and aerosol optical thickness over the oceans with SeaWiFS: A preliminary algorithm, *Appl. Opt.*, 33, 443–452.

Gordon, H. R., and M. Wang (1994b), Influence of oceanic whitecaps on atmospheric correction of ocean-color sensors, *Appl. Opt.*, 33, 7754–7763.

Gordon, H. R., T. Du, and T. Zhang (1997), Remote sensing of ocean color and aerosol properties: resolving the issue of aerosol absorption, *Appl. Opt.*, 36, 8670–8684.

Herman, J. R., P. K. Bhartia, O. Torres, C. Hsu, C. Seftor, and E. Celarier (1997), Global distribution of UV-absorbing aerosols from Nimbus-7/TOMS data, *J. Geophys. Res.*, 102, 16,911–16,922.

Holben, B. N., et al. (1998), AERONET - A federated instrument network and data archive for aerosol characterization, *Remote Sens. Environ.*, 66, 1–16.

Hooker, S. B., W. E. Esaias, G. C. Feldman, W. W. Gregg, and C. R. McClain (1992), An overview of SeaWiFS and ocean colour, in *NASA Technical Memorandum 104566, SeaWiFS Tech. Rep. Ser.*, vol. 1, edited by S. B. Hooker and E. R. Firestone, pp. 24, NASA Goddard Space Flight Cent., Greenbelt, Md.

Hurrell, J. W. (1995), Decadal trend in the North Atlantic Oscillation: Regional temperatures and precipitations, *Science*, 269, 676–679.

Hurrell, J. W., Y. Kushnir, M. Visbeck, and G. Ottersen (2003), An overview of the North Atlantic Oscillation, in *The North Atlantic Oscillation: Climate Significance and Environmental Impact*, *Geophys. Monogr. Ser.*, vol. 134, edited by J. W. Hurrell et al., pp. 1–35, AGU, Washington, D. C.

Intergovernmental Panel on Climate Change (IPCC) (2001), *Climate Change 2001: The Scientific Basis*, Cambridge Univ. Press, New York.

Jamet, C., C. Moulin, and S. Thiria (2004), Monitoring aerosol optical properties over the Mediterranean from SeaWiFS images using a neural network inversion, *Geophys. Res. Lett.*, 31, L13107, doi:10.1029/2004GL019951.

Kaufman, Y. J., D. Tanré, H. R. Gordon, T. Nakalima, J. Lenoble, R. Frouin, H. Grassl, B. M. Herman, M. D. King, and P. M. Teillet (1997), Passive remote sensing of tropospheric aerosol and atmospheric correction of the aerosol effect, *J. Geophys. Res.*, 102, 16,815–16,830.

Kaufman, Y. J., A. Smirnov, B. N. Holben, and O. Dubovik (2001), Baseline maritime aerosol: methodology to derive the optical thickness and scattering properties, *Geophys. Res. Lett.*, 28, 3251–3254.

Kaufman, Y. J., D. Tanré, and O. Boucher (2002), A satellite view of aerosols in the climate system, *Nature*, 419, 215–223.

Kaufman, Y. J., I. Koren, L. Remer, D. Tanré, P. Ginoux, and S. Fan (2005), Dust transport and deposition observed from the Terra-Moderate Resolution Imaging Spectroradiometer (MODIS) spacecraft over the Atlantic Ocean, *J. Geophys. Res.*, 110, D10S12, doi:10.1029/2003JD004436.

King, M. D., Y. J. Kaufman, D. Tanré, and T. Nakajima (1999), Remote sensing of tropospheric aerosols from space: past, present, future, *Bull. Am. Meteorol. Soc.*, 80, 2229–2259.

Krom, M. D., S. Brenner, N. Kress, and I. I. Gordon (1991), Phosphorus limitation of Primary Productivity in the E. Mediterranean sea, *Limnol. Oceanogr.*, 36, 424–432.

Levelt, P. F., et al. (2000), Science objectives of EOSAURA's Ozone Monitoring Instrument (OMI), paper presented at the Quadrennial Ozone Symposium, Int. Ozone Comm., Int. Assoc. for Meteorol. and Atmos. Sci., Sapporo, Japan.

Levin, Z., and E. Ganor (1996), The effects of desert particles on cloud and rain formation in the Eastern Mediterranean, in *The Impact of Desert Dust Across the Mediterranean*, edited by S. Guerzoni and R. Chester, pp. 77–86, Springer, New York.

Li, X., H. Maring, D. L. Savoie, K. Voss, and J. M. Prospero (1996), Dominance of mineral dust in aerosol light-scattering in the North Atlantic trade winds, *Nature*, 380, 416–419.

Loÿe-Pilot, M. D., J. M. Martin, and J. Morelli (1986), Influence of Saharan dust on the rain acidity and atmospheric input to the Mediterranean, *Nature*, 321, 427–428.

Martins, J. V., D. Tanré, L. Remer, Y. J. Kaufman, S. Mattoo, and R. Levy (2002), MODIS Cloud screening for remote sensing of aerosols over the oceans using spatial variability, *Geophys. Res. Lett.*, 29(12), 8009, doi:10.1029/2001GL013252.

Moulin, C., and I. Chiapello (2004), Evidence of the control of summer atmospheric transport of African dust over the Atlantic by Sahel sources from TOMS satellites (1979–2000), *Geophys. Res. Lett.*, 31, L02107, doi:10.1029/2003GL018931.

Moulin, C., F. Dulac, C. E. Lambert, P. Chazette, I. Jankowiak, B. Chatenet, and F. Lavenu (1997a), Long-term daily monitoring of Saharan dust load over ocean using Meteosat ISCCP-B2 data 2: Accuracy of the method and validation using Sun photometer measurements, *J. Geophys. Res.*, 102, 16,959–16,969.

Moulin, C., F. Guillard, F. Dulac, and C. E. Lambert (1997b), Long-term daily monitoring of Saharan dust load over ocean using Meteosat ISCCP-B2 data 1. Methodology and preliminary results for 1983–1994 in the Mediterranean, *J. Geophys. Res.*, 102, 16,947–16,958.

Moulin, C., C. E. Lambert, F. Dulac, and U. Dayan (1997c), Control of atmospheric export of dust from North Africa by the North Atlantic oscillation, *Nature*, 387, 691–694.

Moulin, C., et al. (1998), Satellite climatology of African dust transport in the Mediterranean atmosphere, *J. Geophys. Res.*, 103, 13,137–13,144.

Moulin, C., H. R. Gordon, V. F. Banzon, and R. H. Evans (2001a), Assessment of Saharan dust absorption in the visible from SeaWiFS imagery, *J. Geophys. Res.*, 106, 18,239–18,249.

Moulin, C., H. R. Gordon, R. M. Chomko, V. F. Banzon, and R. H. Evans (2001b), Atmospheric correction of ocean color imagery through thick layers of Saharan dust, *Geophys. Res. Lett.*, 28, 5–8.

Nobileau, D., and D. Antoine (2005), Detection of blue-absorbing aerosols using near infrared and visible (ocean color) remote sensing observations, *Remote Sens. Environ.*, 95, 368–387.

Patterson, E. M. (1981), Optical properties of the crustal aerosol: Relation to chemical and physical characteristics, *J. Geophys. Res.*, 86, 3236–3246.

Prospero, J. M., and T. N. Carlson (1972), Vertical and areal distribution of Saharan dust over the Western Equatorial North Atlantic Ocean, *J. Geophys. Res.*, 77, 5255–5265.

Rast, M., J. L. Bézy, and S. Bruzzi (1999), The ESA Medium Resolution Imaging Spectrometer MERIS–a review of the instrument and its mission, *Int. J. Remote Sens.*, 20, 1681–1702.

Remer, L. A., et al. (2005), The MODIS Aerosol Algorithm, Products and Validation, *J. Atmos. Sci.*, 62, 947–973.

Santoleri, R., G. L. Liberti, G. P. Gobbi, F. Barnaba. M. Ribera d'Alcala, F. D'Ortenzio, M. Ragni, G. L. Volpe, E. Bohm, and S. Marullo (2002), Validation of SeaWiFS ocean and atmospheric products in the Mediterranean sea: NASA SIMBIOS project 2001 annual report, *NASA Tech. Memo. 2002–210005*, edited by G. S. Fargion and C. R. McClain, pp. 176–184, NASA Goddard Space Flight Cent., Md.

Savoie, D. L., and J. M. Prospero (1977), Aerosol concentration statistics for the Northern Tropical Atlantic, *J. Geophys. Res.*, 82, 5954–5964.

Schollaert, S. E., J. A. Yoder, D. L. Westphal, and J. E. O'Reilly (2003), Influence of dust and sulfate aerosols on ocean color spectra and chlorophyll-a concentrations derived from SeaWiFS off the East Coast U.S., *J. Geophys. Res.*, *108*(C6), 3191, doi:10.1029/2000JC000555.

Schwindling, M., P.-Y. Deschamps, and R. Frouin (1998), Verification of aerosol models for satellite ocean color remote sensing, *J. Geophys. Res.*, *103*, 24,919–24,935.

Shettle, E. P., and R. W. Fenn (1979), Models for the aerosols of the lower atmosphere and the effects of humidity variations on their optical properties, *Environ. Res. Pap. 676, AFGL-TR-79–0214*, Air Force Geophys. Lab., Hanscom Air Force Base, Mass.

Stegman, P. M. (2000), Ocean-color satellites and the phytoplankton-dust connection, in *Satellites, Oceanography and Society*, edited by D. Halpern, pp. 207–223, Elsevier, New York.

Stegman, P. M. (2004a), Remote sensing of aerosols with ocean colour sensors: then and now, *Int. J. Remote Sens.*, *25*, 1409–1413.

Stegman, P. M. (2004b), Characterization of aerosols over the North Atlantic ocean from SeaWiFS, *Deep Sea Res. II*, *51*, 913–925.

Stegman, P. M., and N. W. Tindale (1999), Global distribution of aerosols over the open ocean as derived from the coastal zone color scanner, *Global Biogeochem. Cycles*, *13*, 383–397.

Tanré, D., J. Haywood, J. Pelon, J. F. Léon, B. Chatenet, P. Formenti, P. Francis, P. Goloub, E. J. Highwood, and G. Myhre (2003), Measurement and modeling of the Saharan dust radiative impact: overview of the Saharan dust experiment (SHADE), *J. Geophys. Res.*, *108*(D18), 8574, doi:10.1029/2002JD003273.

Torres, O., P. K. Bhartia, J. R. Herman, Z. Ahmad, and J. Gleason (1998), Derivation of aerosol properties from satellite measurements of backscattered ultraviolet radiation: Theoretical basis, *J. Geophys. Res.*, *103*, 17,099–17,110.

Villevalde, Y. V., A. V. Smirnov, N. T. O'Neill, S. P. Smyshlyaev, and V. V. Yakovlev (1994), Measurement of aerosol optical depth in the Pacific ocean and the North Atlantic, *J. Geophys. Res.*, *99*, 20,983–20,988.

Wang, M., S. Bailey, and C. R. McClain (2000), SeaWiFS provides unique global aerosol optical property data, *Eos Trans. AGU*, *81*, 197–202.

Wang, M., K. D. Knobelspiesse, and C. R. McClain (2005), Study of the Sea-Viewing Wide Field-of-View Sensor (SeaWiFS) aerosol optical property data over ocean in combination with the ocean color products, *J. Geophys. Res.*, *110*, D10S06, doi:10.1029/2004JD004950.

World Climate Research Program (WCRP) (1986), A preliminary cloudless standard atmosphere for radiation computation, *WCP-112, WMO/TD-24*, 60 pp., Int. Assoc. for Meteorol. and Atmos. Phys., Boulder, Colo.

————————————

D. Antoine and D. Nobileau, Laboratoire d'Océanographie de Villefranche (LOV, UMR 7093), Observatoire Océanologique de Villefranche, CNRS/Université Pierre et Marie Curie-Paris 6, F-06230 Villefranche sur mer, France. (antoine@obs-vlfr.fr)